

1 Submitted to *Monthly Weather Review*, March 30, 2011

2 September, 15, 2011 version with corrected Fig. 1

3 **Implicit-Explicit Multistep Methods for Fast-Wave Slow-Wave**
4 **Problems**

5 DALE R. DURRAN * AND PETER N. BLOSSEY

University of Washington, Seattle, Washington, USA

* *Corresponding author address:* Dale R. Durran, University of Washington, Atmospheric Sciences, Box 351640, Seattle, WA 98195-1640

E-mail: drdee@uw.edu

7 Implicit-explicit (IMEX) linear multistep methods are examined with respect to their suit-
8 ability for the integration of fast-wave, slow-wave problems in which the fast wave has rel-
9 atively low amplitude and need not be accurately simulated. The widely used combination
10 of trapezoidal implicit and leapfrog explicit differencing is compared to schemes based on
11 Adams methods or on backward differencing. Two new families of methods are proposed
12 that have good stability properties in fast-wave, slow-wave problems: one family is based on
13 Adams methods and the other on backwards schemes. We focus primarily on four specific
14 schemes drawn from these two families: a pair of Adams methods and a pair of backwards
15 methods which are either i) optimized for third-order accuracy in the explicit component of
16 the full IMEX scheme, or ii) employ particularly good schemes for the implicit component.
17 These new schemes are superior, in many respects, to the linear multistep IMEX schemes
18 currently in use.

19 The behavior of these schemes is compared theoretically in the context of the simple
20 oscillation equation and also for the linearized equations governing stratified compressible
21 flow. Several schemes are also tested in fully nonlinear simulations of gravity waves generated
22 by a localized source in a shear flow.

23 1. Introduction

24 The atmosphere and the ocean support several different types of waves that propagate
25 at very different speeds. If time derivatives in the equations governing atmospheric flow are
26 approximated using explicit finite difference schemes, the maximum stable time step will
27 be limited by the speed of the fastest moving wave. Yet the fastest moving atmospheric
28 and oceanic waves are sound waves, which play no direct role in atmospheric and ocean
29 circulations and do not need to be accurately simulated.

30 Atmospheric models typically avoid the severe time-step restrictions associated with
31 sound wave propagation in one of three ways. One approach is to replace the governing
32 equations with an approximate system, such as the anelastic (Ogura and Phillips 1962;
33 Lipps and Hemler 1982; Bannon 1996), or pseudo-incompressible equations (Durran 1989,
34 2008), before constructing any numerical approximations. The other two approaches approx-
35 imate the full compressible equations using numerical techniques that treat sound waves in
36 a stable, but inaccurate manner, while faithfully approximating the behavior of the slower
37 moving waves. This may be accomplished either by resorting to implicit time differencing
38 (Tapp and White 1976) or by splitting up the terms in the governing equations and integrat-
39 ing those responsible for sound wave propagation on a smaller time step than that used for
40 the remaining terms (Klemp and Wilhelmson 1978; Tatsumi 1983; Wicker and Skamarock
41 2002).

42 Fully implicit time differences require the solution of a nonlinear algebraic system at each
43 time step, and while they continue to be the subject of ongoing investigation (Evans et al.
44 2010), they are generally thought to be less efficient than implicit-explicit (IMEX) methods
45 (also known as semi-implicit methods) in which only those terms responsible for linear sound
46 wave propagation are evaluated using implicit differences and the remaining terms are inte-
47 grated using explicit formulae. A large body of research exists on the construction of IMEX
48 methods for advection-diffusion problems, in which the diffusion terms are treated implicitly
49 and the advection terms with some type of explicit differencing (Varah 1980; Ascher et al.
50 1995). Less attention has been devoted to the development of IMEX methods for fast-wave
51 slow-wave problems, but at least in atmospheric science, a basic leapfrog-trapezoidal IMEX
52 method (see first line of Table 1) is widely used (Kwizak and Robert 1971) .

53 Consistent with the true solution, pure IMEX leapfrog-trapezoidal approximations to
54 inviscid linear wave-propagation problems neither damp nor amplify the numerical solution.
55 In practical applications, however, the leapfrog-trapezoidal method requires some modifi-

56 cations. The computational mode of the explicit leapfrog scheme is undamped and may
 57 interact with the physical mode in nonlinear problems to produce spurious $2\Delta t$ oscilla-
 58 tions (time-splitting); Robert-Asselin (RA) filtering (Robert 1966; Asselin 1972) or Robert-
 59 Asselin-Williams (RAW) filtering (Williams 2009) is often applied to avoid this problem. In
 60 addition, the weights in the trapezoidal integration formula are sometimes backward biased
 61 in an effort to enhance the stability of the implicit part (Benoit et al. 1997), by choosing
 62 $1/2 < \theta \leq 1$ in the formula given on the first line of Table 1. Either filtering or off-
 63 centering the integration weights renders these methods first-order accurate. In addition
 64 the off-centering damps a rather wide range of frequencies, including those that are rather
 65 well-resolved. Can we do better?

66 The leapfrog-trapezoidal method is a linear multistep IMEX method. In the following we
 67 explore several other linear multistep methods that lend themselves to IMEX differencing in
 68 fast-wave slow-wave problems while producing more scale-selective damping at the highest
 69 frequencies. These methods permit almost the same maximum stable time step allowed by
 70 the filtered IMEX leapfrog-trapezoidal methods while achieving higher accuracy.

71 **2. Formulation of IMEX Multistep Methods**

72 The equations governing atmospheric or ocean dynamics (and many other processes) can
 73 be expressed in the form

$$\frac{\partial \mathbf{u}}{\partial t} = \mathbf{f}(\mathbf{u}) + \mathbf{L}\mathbf{u}, \quad (1)$$

74 where \mathbf{u} is the state variable, \mathbf{L} is the matrix associated with a linear operator that includes
 75 processes with short timescales (such as sound and/or gravity wave propagation), and all
 76 remaining terms are collected in $\mathbf{f}(\mathbf{u})$, including those responsible for advection. If the terms
 77 supporting the fast processes are not linear, they may be linearized to form \mathbf{L} , and the
 78 remaining nonlinear contributions may be incorporated in \mathbf{f} .

79 Letting \mathbf{q}^n be the numerical approximation to \mathbf{u} at time $n\Delta t$, a linear IMEX $M + 1$ step
 80 approximation to (1) may be expressed in the form

$$\sum_{k=-M}^1 \alpha_k \mathbf{q}^{n+k} = \Delta t \left[\sum_{k=-M}^0 \beta_k \mathbf{f}(\mathbf{q}^{n+k}) + \sum_{k=-M}^1 \nu_k \mathbf{L} \mathbf{q}^{n+k} \right]. \quad (2)$$

81 The set of coefficients (α_k, β_k) define the explicit method, whereas the implicit portion is
 82 defined by the set (α_k, ν_k) . The use of a single set of α_k restricts the choice of explicit and
 83 implicit multistep methods that can be combined in the IMEX scheme to those with identical
 84 α_k .

85 *a. The implicit component*

86 To ensure that the time step is not restricted by the fast processes, the implicit method
 87 should be A -stable, although as shown by Dahlquist (1963) no A -stable linear multistep
 88 method can be higher than second-order accurate. A method is A -stable if when applied to
 89 the scalar problem

$$\frac{du}{dt} = \eta u, \quad (3)$$

90 with u and η complex, and $\Re\{\eta\} \leq 0$, the magnitude of the factor by which the numerical
 91 solution amplifies each time step, $|A| \equiv |q^{n+1}/q^n|$, is bounded by unity regardless of the size
 92 of the time step (Durrant 2010, p. 41).¹ When IMEX methods are used in advection-diffusion
 93 problems, the implicit method typically has the additional property that it is L -stable. An
 94 L -stable method is an A -stable method satisfying the additional condition that $|A| \rightarrow 0$
 95 as $\Re\{\eta\}\Delta t \rightarrow -\infty$ (Durrant 2010, p. 48). Integrating the diffusion terms with an L -stable
 96 method ensures that very short wavelength features decay properly when the time step
 97 and the diffusivities are large. Some damping of the highest frequencies has also proved

¹An N -step linear multistep method has N amplification factors, one of which corresponds to the physical mode. The others are associated with computational modes. Unless specified otherwise, $|A|$ will refer to the maximum of the magnitude of the amplification factor over all physical and computational modes.

98 helpful in many fast-wave slow-wave problems, so here our primary focus will be on implicit
 99 methods that provide such damping, although we will not necessarily require $|A| \rightarrow 0$ as
 100 $\Im\{\eta\}\Delta t \rightarrow \pm\infty$.

101 One set of potentially attractive candidates for use in linear IMEX multistep meth-
 102 ods are the Adams schemes for which $\alpha_1 = 1$, $\alpha_0 = -1$ and $\alpha_k = 0$ for $-M \leq k < 0$.
 103 The highest-order explicit Adams scheme that can be obtained using s steps is the s -step
 104 Adams-Bashforth method; the highest-order implicit scheme is the s -step Adams-Moulton
 105 method. Adams-Moulton implicit schemes are, however, of limited use in IMEX formula-
 106 tions because the only A -stable Adams-Moulton method is the classical one-step trapezoidal
 107 scheme (denoted here as T1), which does not damp high frequency oscillations. We will
 108 therefore consider Adam's methods whose order of accuracy is lower than the best that can
 109 be achieved using a given number of time steps, but whose stability properties nevertheless
 110 make them potential attractive choices for IMEX approximations to fast-wave/slow-wave
 111 problems.

112 The simplest example of such a method may be obtained from the trapezoidal scheme,
 113 which may be modified to produce frequency-dependent damping by off-centering it in time;
 114 the result is a first-order one-step scheme. When used in conjunction with an explicit leapfrog
 115 scheme, the time differencing in the two schemes is made compatible by approximating the
 116 trapezoidal difference over $2\Delta t$ (in which case it is not formally an Adams scheme). The
 117 result is

$$\frac{\mathbf{q}^{n+1} - \mathbf{q}^{n-1}}{2\Delta t} = \theta \mathbf{L}\mathbf{q}^{n+1} + (1 - \theta)\mathbf{L}\mathbf{q}^{n-1}, \quad (4)$$

118 with $1/2 < \theta \leq 1$. Choosing θ near $1/2$ gives the best accuracy, but only weak damping.
 119 We will refer to this scheme as T2 θ .

120 Second-order accuracy can be achieved using a member of the following one-parameter
 121 family of implicit Adams methods, which are A -stable for any non-negative c (Frank et al.

122 1997).

$$\frac{\mathbf{q}^{n+1} - \mathbf{q}^n}{\Delta t} = \frac{1}{2}(1+c)\mathbf{L}\mathbf{q}^{n+1} + \frac{1}{2}(1-2c)\mathbf{L}\mathbf{q}^n + \frac{c}{2}\mathbf{L}\mathbf{q}^{n-1} \quad (5)$$

123 Choosing $c = 0$ reduces this to a two-step method and gives the familiar trapezoidal scheme.
 124 The case $c = 1/2$ yields the method denoted AM2* by Fornberg and Driscoll (1999), who
 125 used it in conjunction with a fourth-order Adams-Bashforth method for IMEX simulations
 126 of dispersive waves. Nevanlinna and Liniger (1978) found AM2* to be the two-step second-
 127 order method that gave the smallest error bounds among all methods that yield non-growing
 128 solutions to a test problem similar to (3) with $\eta(t) \leq \eta_0 < 0$ for $t \geq 0$.

129 Instead of Adams methods, one could alternatively consider the one-parameter family of
 130 backward methods

$$\frac{\frac{3}{2}\mathbf{q}^{n+1} - 2\mathbf{q}^n + \frac{1}{2}\mathbf{q}^{n-1}}{\Delta t} = (1+c)\mathbf{L}\mathbf{q}^{n+1} - 2c\mathbf{L}\mathbf{q}^n + c\mathbf{L}\mathbf{q}^{n-1}. \quad (6)$$

131 The left-hand side is the standard second-order backward-difference approximation to the
 132 derivative at time level $n + 1$ and the right-hand side is a second order approximation to $\mathbf{L}\mathbf{q}$
 133 at time $n + 1$. The familiar L -stable second-order backward difference formula (BDF2) is
 134 obtained by choosing $c = 0$. Numerical evaluations of the amplification factor A show the
 135 family schemes (6) to be A -stable for $c \geq -1/4$.

136 The amplification factors A generated by several of the preceding implicit methods are
 137 compared with that for the exact solution to (3) in Fig. 1. Each panel shows contours of
 138 $|A|$ plotted as a function of $\Re\{\eta\}\Delta t$ and $\Im\{\eta\}\Delta t$. Method AI2* is (5) with $c = 3/2$, method
 139 BI2* is (6) with $c = 1/3$; the significance of these methods will be discussed in Section 3.

140 As expected for A -stable methods, $|A| \leq 1$ throughout the half-plane $\Re\{\eta\}\Delta t \leq 0$. One
 141 limiting behavior is exhibited by the T2 θ method with $\theta = 0.5$, which correctly preserves
 142 the amplitude of purely oscillatory solutions, but fails to correctly damp the solution
 143 if $\Re\{\eta\}\Delta t \ll -1$. The other limit is attained by the BDF2 method, which consistent with
 144 its L -stability, provides the best treatment of the strongly damped case ($\Re\{\eta\}\Delta t \ll -1$).

145 Most of the other methods produce significant damping as $\Re\{\eta\}\Delta t \rightarrow -\infty$ (the values of
 146 $|A|$ in this limit appear in the lower left corner of each panel of Fig. 1), and like BDF2,
 147 they preserve the amplitude of purely oscillatory motions for $|\Im\{\eta\}\Delta t|$ less than about 1/2.
 148 The exception is the T2 θ method with $\theta = 0.6$, which requires the smallest time step in the
 149 purely oscillatory case to avoid spurious damping, yet fails to produce strong damping when
 150 $\Re\{\eta\}\Delta t \rightarrow -\infty$.

The damping and phase errors for each of these methods is examined in detail for the purely oscillatory case ($\Re\{\eta\} = 0$), in Fig. 2. The frequency dependence of the damping is indicated by the plot of $|A|$ as a function of $\Im\{\eta\}\Delta t$ in Fig. 2a. All the methods preferentially damp the poorly resolved waves, except for T2 θ with $\theta = 0.5$, which correctly preserves the amplitude of the solution. The AM2* method is the second best at preserving the amplitude, the least frequency-selective method is T2 θ with $\theta = 0.6$. The relative phase error

$$R = \frac{1}{\Im\{\eta\}\Delta t} \arctan\left(\frac{\Im\{A\}}{\Re\{A\}}\right),$$

151 is plotted as a function of $\Im\{\eta\}\Delta t$ in Fig. 2b; R is the ratio of the phase advance produced
 152 by one step of the numerical scheme to the phase advance in the exact solution of (3) over
 153 the same time interval. The smallest phase errors are produced by the BDF2 method. AM2*
 154 and the T2 θ methods also perform relatively well.² The largest phase errors are generated
 155 by the AI2* scheme; the BI2* method is the second worst.

156 *b. The explicit component*

157 When the implicit part of a multi-step IMEX scheme is approximated using the modified
 158 trapezoidal scheme (4), the explicit part of the integration is often performed using the
 159 leapfrog scheme with Robert-Asselin filtering (Robert 1966; Asselin 1972). Williams (2009,
 160 2011) recently proposed an improvement to this filter, the resulting ‘‘RAW-filtered’’ leapfrog

²T1, the standard trapezoidal method, in which the time difference is computed over an interval of Δt rather than $2\Delta t$ as in (4), would give the lowest phase error.

161 scheme has the form

$$\frac{\mathbf{q}^{n+1} - \tilde{\mathbf{q}}^{n-1}}{2\Delta t} = \mathbf{f}(\tilde{\mathbf{q}}^n) \quad (7)$$

$$\tilde{\mathbf{q}}^n = \tilde{\mathbf{q}}^n + \frac{\sigma\gamma}{2} (\tilde{\mathbf{q}}^{n-1} - 2\tilde{\mathbf{q}}^n + \mathbf{q}^{n+1}) \quad (8)$$

$$\tilde{\mathbf{q}}^{n+1} = \mathbf{q}^{n+1} + \frac{(\sigma-1)\gamma}{2} (\tilde{\mathbf{q}}^{n-1} - 2\tilde{\mathbf{q}}^n + \mathbf{q}^{n+1}). \quad (9)$$

162 Here $\tilde{\mathbf{q}}$ represents a provisional singly filtered value and $\tilde{\tilde{\mathbf{q}}}$ the doubly filtered final value of
 163 \mathbf{q} , while γ and σ are constant filter parameters.³ The original Robert-Asselin formulation
 164 (with filter coefficient $\gamma/2$) is obtained by setting $\sigma = 1$. Here we use $\sigma = 0.53$ in the
 165 RAW filter following Williams (2009). Depending on the nonlinearity of the underlying
 166 problem, time-splitting instability is typically avoided by choosing a value of γ the range
 167 $0.05 \leq \gamma/2 \leq 0.2$.

168 Adams-Bashforth methods are obvious possibilities for the explicit part of multistep
 169 IMEX schemes which use an implicit Adams method. The two-step Adams-Bashforth
 170 method is a poor choice because it amplifies oscillatory solutions, but the three-step method,
 171 hereafter denoted AB3, generally gives good results and is also third-order accurate. As with
 172 was the case for implicit Adams methods, for fast-wave/slow-wave IMEX applications, it will
 173 be useful to consider the family of three-step methods that are at least second-order accurate.
 174 This one-parameter family may be expressed in the form

$$\frac{\mathbf{q}^{n+1} - \mathbf{q}^n}{\Delta t} = \frac{1}{2}(3+b)\mathbf{f}(\mathbf{q}^n) - \frac{1}{2}(1+2b)\mathbf{f}(\mathbf{q}^{n-1}) + \frac{b}{2}\mathbf{f}(\mathbf{q}^{n-2}). \quad (10)$$

175 The two-step and three-step Adams-Bashforth schemes are obtained by choosing $b = 0$ and
 176 $b = 5/6$, respectively.

177 Suitable explicit methods for use with the implicit backward schemes (6) are less well
 178 known. The one-parameter family of three-step explicit backward schemes of at least second-
 179 order accuracy has the form

$$\frac{\frac{3}{2}\mathbf{q}^{n+1} - 2\mathbf{q}^n + \frac{1}{2}\mathbf{q}^{n-1}}{\Delta t} = (2+b)\mathbf{f}(\mathbf{q}^n) - (1+2b)\mathbf{f}(\mathbf{q}^{n-1}) + b(\mathbf{q}^{n-2}) \quad (11)$$

³When the RAW filter is used in leapfrog-trapezoidal IMEX schemes, $\tilde{\mathbf{q}}^{n-1}$ replaces \mathbf{q}^{n-1} in (4)

180 Choosing $b = 0$ yields a method that seen use in combination with BDF2 to obtain second-
 181 order IMEX methods (Karniadakis et al. 1991; Giraldo et al. 2010)⁴. The $b = 0$ method,
 182 which we will denote BX2, does have the disadvantage that it erroneously amplifies purely
 183 oscillatory solutions. The choice $b = 2/3$ gives a third-order method that will be denoted
 184 BX3*; this method is the explicit component of the IMEX BDF2B scheme of Giraldo (2005),
 185 who attributed it to Hulsten.

186 Fig. 3 shows $|A|$ for selected explicit methods in the same format as Fig. 1. AX2* and
 187 BX2* correspond to the choice $b = 1/2$ in (10) and (11), respectively. The significance of
 188 these two schemes will be discussed in the next section. As is well known, the region for
 189 which the unfiltered leapfrog scheme generates non-growing solutions is the segment $(-1, 1)$
 190 along the imaginary axis of the $\Re\{\eta\}\Delta t - \Im\{\eta\}\Delta t$ plane. Both the Asselin-Robert and the
 191 RAW filter widen this region somewhat, while decreasing the maximum values of $\Im\{\eta\}\Delta t$
 192 for which $|A| \leq 1$. Nevertheless, the filtered leapfrog schemes remain far less suited to the
 193 simulation of damping processes than the other explicit methods shown in Fig. 3. The best
 194 scheme for simulating problems with some dissipation is BX2*, which in the $\Im\{\eta\}\Delta t = 0$
 195 case, does a good job of approximating the correct rate of damping for $-0.5 \leq \Re\{\eta\}\Delta t \leq 0$
 196 and remains stable for $\Re\{\eta\}\Delta t$ as negative as roughly -0.9.

197 Further details about the amplification factor for the oscillatory case are shown by the
 198 plot of $|A|$ as a function of $\Im\{\eta\Delta t\}$ in Fig. 4a for the physical mode associated with each
 199 of the preceding explicit schemes as well as BX2, which is the previously used version of
 200 (11) for which $b = 0$. The unstable amplification generated by BX2 is clearly apparent,
 201 as is the weaker damping produced by all other methods except the RAW filtered leapfrog
 202 scheme. The RAW filtered leapfrog scheme (with $\gamma = 0.2$ and $\sigma = 0.53$) generates very
 203 weak damping for $0 \leq \Im\{\eta\Delta t\} \leq \sim 0.42$, and weak amplification at larger time steps. The
 204 stability limits for AB3 and BX3* arise when the amplification factor for one of their two

⁴Varah (1980) and Frank et al. (1997) considered a variant of this method in which the right side is replaced by $\mathbf{f}(2\mathbf{q}^n - \mathbf{q}^{n-1})$, which is equivalent to (11) with $b = 0$ when \mathbf{f} is linear.

205 computational modes exceeds unity. Values of $|A|$ for the computational modes associated
 206 with the preceding schemes are plotted in Fig. 4b. Among all these methods, AB3 clearly
 207 produces the smallest relative phase errors (Fig. 4c).

208 3. Stability analysis of IMEX methods

209 a. The oscillation equation

210 In the preceding Section, the properties of the implicit and explicit methods were consid-
 211 ered in isolation, but these methods interact in complex ways when combined in an IMEX
 212 time integration scheme. For example, despite their attractive properties, the third-order
 213 Adams-Bashforth method and trapezoidal method combine to form a IMEX method that is
 214 of little use in fast-wave slow-wave problems (Durran 1991). The stability of IMEX approx-
 215 imations to fast-wave slow-wave problems can be explored using a variant of the oscillation
 216 equation

$$\frac{\partial q}{\partial t} = i\omega_L q + i\omega_H q, \quad (12)$$

217 where the the frequencies ω_H and ω_L represent the oscillations triggered by the propagation
 218 of fast and slow waves, respectively.

219 As an example of the analysis, the explicit-implicit AI2*/AB3 approximation to (12)
 220 takes the form

$$\begin{aligned} \frac{q^{n+1} - q^n}{\Delta t} = & i\omega_L \left(\frac{23}{12} q^n - \frac{4}{3} q^{n-1} + \frac{5}{12} q^{n-2} \right) \\ & + i\omega_H \left(\frac{5}{4} q^{n+1} - q^n + \frac{3}{4} q^{n-1} \right), \end{aligned} \quad (13)$$

221 and the amplification factor A for this method satisfies

$$\begin{aligned} \left(1 - \frac{5}{4} i\omega_H \Delta t \right) A^3 + \left(-1 - \frac{23}{12} i\omega_L \Delta t + i\omega_H \Delta t \right) A^2 \\ + \left(\frac{4}{3} i\omega_L \Delta t - \frac{3}{4} i\omega_H \Delta t \right) A - \frac{5}{12} i\omega_L \Delta t = 0. \end{aligned} \quad (14)$$

222 The amplification factors for the other methods listed in Table 1 were computed in a similar
 223 manner. The only complication arises in the analysis of the Asselin-filtered leapfrog scheme,
 224 where it is assumed that $\widetilde{A}\mathbf{q} = A\tilde{\mathbf{q}}$ and $\widetilde{A}\tilde{\mathbf{q}} = A\tilde{\tilde{\mathbf{q}}}$ (see Durran 2010, p. 65).

225 The magnitudes of the amplification factors for several variants of the leapfrog-T2 θ
 226 schemes are contoured as a function of $\omega_L\Delta t$ and $\omega_H\Delta t$ in Fig. 5. The result for $\theta = 1/2$,
 227 $\gamma = 0$ (Fig. 5a) is excellent in the sense that (a) the scheme is stable for all values of Δt
 228 provided $|\omega_L| < |\omega_H|$ (because $|A| \leq 1$ in the wedge-shaped region $|\omega_L\Delta t| < |\omega_H\Delta t|$), and
 229 (2) even in the case $|\omega_L| > |\omega_H|$, the stability of the method is limited exclusively by the ex-
 230 plicitly differenced term (because $|A| \leq 1$ in the vertical strip $|\omega_L\Delta t| < 1$). Off-centering the
 231 implicit term by choosing $\theta = 0.6$ (Fig. 5b) preserves stability throughout the wedge-shaped
 232 region $|\omega_L\Delta t| < |\omega_H\Delta t|$, but does significantly reduce the range of $\omega_L\Delta t$ over which stable
 233 solutions can be obtained when $\omega_H\Delta t$ is small—a counter-intuitive result since off-centering
 234 the trapezoidal method adds damping which might be supposed to increase stability.

235 As mentioned previously, a serious difficulty with the pure leapfrog scheme is that, in
 236 nonlinear problems, the solution may be subject to time-splitting instability. When $\theta = 0.5$,
 237 using the Robert-Asselin (RA) filter ($\sigma = 1$ in (8)–(9)) with $\gamma = 0.2$, produces only a modest
 238 influence on the geometry of the stable region for small values of $\omega_H\Delta t$, but does restrict the
 239 stability condition for larger time steps, since $|\omega_L| < 1.22|\omega_H|$ becomes the corresponding
 240 stability condition for arbitrary Δt (cf. Fig. 5a,c). A similar modest reduction in stability
 241 is produced by increasing γ from 0 to 0.2 if the implicit scheme is off-centered with $\theta = 0.6$
 242 (cf. Fig. 5b,d). The stability condition $|\omega_L\Delta t| < |\omega_H\Delta t|$ is recovered when the new RAW
 243 filter is used (with $\sigma = 0.53$ and $\gamma = 0.2$) instead of the RA filter, but there is a reduction
 244 in stability when $\omega_H\Delta t$ is small (for both θ values).

245 Two parameters describing simple aspects of the stability region for the T2 θ /LF scheme
 246 are listed in Table 2: μ characterizes the stability when no high frequency oscillation is
 247 present in the sense that stability is guaranteed if $|\omega_L\Delta t| < \mu$ and $|\omega_H\Delta t| = \epsilon$, where

248 $\epsilon > 0$ is an arbitrarily small constant.⁵ In contrast, ξ is the smallest value for which stable
 249 solutions may be obtained regardless of the value Δt provided $|\omega_L| < \xi|\omega_H|$; as such, it
 250 characterizes the spread of the widest wedge-shaped subset of the region of unconditional
 251 stability emanating upward from the origin.

252 The magnitudes of the amplification factors for the other methods listed in Table 1, are
 253 shown in Fig. 6,⁶ and the values of μ and ξ for these methods are also listed in Table 2. The
 254 T1/AB3 combination (Fig. 6a) has a very small region of stability, and as noted in Durran
 255 (1991), is not suitable for fast-wave slow-wave problems. In particular, $\mu = 0$ and $\xi = \infty$ for
 256 the T1/AB3 scheme. The previously used combination BDF2/BX2 (Fig. 6b) requires the
 257 frequency of the fast oscillation to dominate that of the slow oscillation by the factor $\xi = 3$,
 258 which is considerably worse than the values of ξ for the leapfrog-trapezoidal-based methods,
 259 but not worse than that for some of the other schemes shown in Fig. 6. The stability of the
 260 BDF2/BX2 method is, however, poor in the case where $|\omega_H\Delta t|$ is small, indeed $\mu = 0$ for
 261 this method.

262 Near the origin in the $\omega_L\Delta t$ - $\omega_H\Delta t$ plane, the geometry of the regions of instability in
 263 IMEX multi-step methods often includes the line $\omega_H\Delta t = -\omega_L\Delta t$ (as in Figs. 5d and 6a,b).
 264 In addition, the region of stability along the line $\omega_H\Delta t = 0$ can also be quite limited. We
 265 therefore conducted an empirical search for those combinations of IMEX Adams schemes
 266 and those combinations of IMEX backward schemes that were stable along the piecewise
 267 linear curve

$$\omega_H\Delta t = 1/2 - |\omega_L\Delta t|, \quad \omega_L\Delta t \in [-1/2, 1/2]. \quad (15)$$

268 This curve is indicated by the heavy black line in each panel of Fig. 6.

269 The criteria for stable IMEX schemes along this segment proved surprisingly simple.
 270 IMEX Adams schemes, formed by combining (5) and (10), give stable approximations to

⁵The case $\epsilon = 0$ is not included because, for many schemes that are unstable arbitrarily close to the origin, $|A| \rightarrow 1$ as $|\omega_H\Delta t| \rightarrow 0$.

⁶Discussion of the MCN/AX2+ scheme, listed in Table 1, will be deferred until the Conclusions.

271 (12) for all $(\omega_L \Delta t, \omega_H \Delta t)$ along (15) provided b and c satisfy

$$c = 3b + 1, \quad 0.105 < c < 3.85. \quad (16)$$

272 We do not have an analytic proof that this is the optimal relation between b and c , but it
273 does seem likely that the coefficients defining the relation are actually the preceding integers.
274 If the intercept in (15) was perturbed by just ± 0.01 it was not possible to find any values
275 of b or c for which the resulting IMEX Adams method was stable for all points along the
276 segment (15). In a similar way, the optimal combination of backward schemes (6) and (11)
277 was empirically determined to be

$$c = 2b + 1, \quad -0.158 < c < 2.00. \quad (17)$$

278 Once again, this result is robust to perturbation of the intercept by values of ± 0.01 and
279 larger.

280 What criteria might we use to choose among the members of these one-parameter families
281 of stable Adams and backward IMEX methods for fast-wave/slow-wave problems? In cases
282 where the fast wave is low amplitude and of essentially no physical significance (e.g., sound
283 waves), the best accuracy can often be obtained using the value of b associated with the
284 third-order explicit scheme. This yields the methods AI2*/AB3 and BI2*/BX3* shown in
285 Fig. 6e,f. In comparison with the other methods shown in Fig. 6, both of these methods
286 have relatively large stability regions. In particular, the AI2*/AB3 scheme is unconditionally
287 stable throughout the relatively wide wedge defined by $\xi = 1.23$. Furthermore, like the
288 centered ($\theta = 0.5$) variant of the T2 θ /LF scheme, whenever $|\omega_L| > |\omega_H|$ the stability of
289 AI2*/AB3 combination is limited exclusively by the explicitly differenced term (i.e., $\mu =$
290 0.72).

291 Alternatively, if an accurate treatment of the implicitly approximated terms is important,
292 which may be the case when most of the terms fundamental to gravity wave propagation
293 are treated implicitly, it can be advantageous to choose the most accurate implicit scheme

294 available, and then select a compatible explicit method using (16) or (17). For Adams
 295 methods, following Nevanlinna and Liniger (1978), we propose AM2* as the implicit scheme,
 296 and for the implicit backward method we use classical L -stable BDF2. Among the schemes
 297 plotted in Fig. 2, BDF2 and AM2* produce the smallest phase errors, while the largest errors
 298 are produced by BI2* and AI2*. In addition, the amplitude errors generated by AM2* are
 299 smaller than those from AI2*, and those created by BDF2 are smaller than the ones from
 300 BI2*. The stability regions for the resulting combinations, AM2*/AI2* and BDF2/BX2*
 301 are shown in Fig. 6c,d, respectively. Values of μ and ξ for all these schemes are also given
 302 in Table 2.

303 *b. The Euler equations*

304 The oscillation equation provides a simple prototype problem that is helpful for assessing
 305 the basic behavior of IMEX methods. In practical applications, many waves may be present,
 306 they may move at a variety of different speeds, and several processes may be responsible
 307 for propagating each individual wave. To examine the behavior of the IMEX multistep
 308 methods in a more realistic fluid dynamical context, consider the linearized two-dimensional
 309 “compressible Boussinesq system” (Durrant 2010, p. 409)

$$\left(\frac{\partial}{\partial t} + U\frac{\partial}{\partial x}\right)u + \underbrace{\frac{\partial P}{\partial x}}_s = 0, \quad (18)$$

$$\left(\frac{\partial}{\partial t} + U\frac{\partial}{\partial x}\right)w + \underbrace{\frac{\partial P}{\partial z}}_s = \underbrace{b}_b, \quad (19)$$

$$\left(\frac{\partial}{\partial t} + U\frac{\partial}{\partial x}\right)b + \underbrace{N^2 w}_b = 0, \quad (20)$$

$$\left(\frac{\partial}{\partial t} + U\frac{\partial}{\partial x}\right)P + \underbrace{c_s^2 \left(\frac{\partial u}{\partial x} + \frac{\partial w}{\partial z}\right)}_s = 0. \quad (21)$$

310 Here U is the constant mean horizontal wind speed, u and w are the perturbation horizontal
 311 and vertical wind speeds, and c_s is the speed of sound. The reference-state pressure $\bar{p}(z)$ is
 312 assumed to be in hydrostatic balance with the reference-state density $\bar{\rho}(z)$, and the buoyancy
 313 b , Boussinesq pressure potential P , and Brunt-Väisälä frequency N are defined such that

$$b = -g \frac{\rho - \bar{\rho}(z)}{\rho_0}, \quad P = \frac{p - \bar{p}(z)}{\rho_0}, \quad N^2 = -\frac{g}{\rho_0} \frac{d\bar{\rho}}{dz}, \quad (22)$$

314 where ρ_0 is constant representative value for the density.

315 Let (u_0, w_0, b_0, P_0) be complex valued amplitudes for the prognostic variables (u, w, b, P) .

316 Then wavelike solutions to (18)–(21) of the form

$$\Re\{(u_0, w_0, b_0, P_0)e^{i(kx+lz-\omega t)}\} \quad (23)$$

317 exist provided k and l , the wavenumbers in the x and z directions, and ω , the frequency,
 318 satisfy the dispersion relation

$$(\omega - Uk)^2 = \frac{c_s^2}{2} \left(k^2 + l^2 + \frac{N^2}{c_s^2} \pm \left[\left(k^2 + l^2 + \frac{N^2}{c_s^2} \right)^2 - \frac{4N^2k^2}{c_s^2} \right]^{1/2} \right), \quad (24)$$

319 The positive root in (24) is associated with sound waves, which remain non-trivial solutions
 320 in the limit $N \rightarrow 0$. The pressure-gradient and divergence terms fundamental to sound-wave
 321 propagation are indicated by under-braces labeled ‘s’ in (18), (19) and (21). The negative
 322 root in (24) is associated with gravity (or buoyancy) waves. The forces fundamental to
 323 gravity wave propagation again include pressure gradient forces, as well as the processes
 324 involving buoyancy indicated by the terms with under-braces labeled ‘b’ in (19) and (20).
 325 Both sound and gravity waves are also transported by the mean wind through advection,
 326 which is represented by the terms involving the factor U in (18)–(21).

327 In atmospheric applications⁷, $N^2/c_s^2 \ll l^2$ and, as discussed in Durran (2010, p. 412), the
 328 frequencies corresponding to gravity waves in (24) are well approximated by the relation

$$\omega = Uk \pm \frac{Nk}{(k^2 + l^2 + N^2/c_s^2)^{1/2}}. \quad (25)$$

⁷For example, if $N = 0.01 \text{ s}^{-1}$ and $c_s = 300 \text{ m s}^{-1}$, N^2/c_s^2 can be neglected in comparison with l^2 unless the vertical wavelength exceeds 100 km.

329 The frequency increases as the vertical wavelength increases ($l \rightarrow 0$) or the horizontal wave-
 330 length decreases ($k \rightarrow \infty$), and is bounded by $|Uk_{\max}| + N$, where k_{\max} is the maximum
 331 horizontal wave-number (corresponding to the shortest horizontal wavelength) retained on
 332 the spatial mesh. A sufficient condition for the stability of the gravity wave modes in a
 333 *completely explicit* approximation typically takes the form

$$(|Uk_{\max}| + N)\Delta t < C, \quad (26)$$

334 where C is a constant of order unity whose precise value depends on the numerical integrator.
 335 For the leapfrog scheme without time filtering, $C = 1$, for AB3 $C = 0.72$, and for BX2*
 336 $C = 0.67$.

337 Under the same approximation that $N^2/c_s^2 \ll l^2$, the frequencies for the sound waves are
 338 well approximated as

$$\omega^2 = c_s^2 (k^2 + l^2 + N^2/c_s^2). \quad (27)$$

339 Letting $\kappa^2 = k^2 + l^2$ and again neglecting the term N^2/c_s^2 , the stability condition for the
 340 sound wave modes in a completely explicit approximation typically takes the form

$$c_s \kappa_{\max} \Delta t < C. \quad (28)$$

341 Here κ_{\max} is the maximum total wave-number (associated with the shortest wavelength)
 342 retained on the spatial mesh, and C is again a constant dependent on the numerical inte-
 343 grator. For the the pure leapfrog scheme, AB3, and BX2*, C takes the same specific values
 344 previously mentioned in connection with (26). The stability restriction for the sound waves
 345 (28) is typically much more severe than that for the gravity waves (26), because the vertical
 346 resolution in atmospheric models is typically much finer than the horizontal resolution and
 347 c_s is large.

348 To allow a larger time step than that required to stabilize the sound waves, first consider
 349 IMEX approximations to (18)–(21) in which the terms labelled ‘s’ are treated implicitly, and
 350 all the remaining terms are stepped forward with an explicit scheme. The quantities defined

351 in (1) become

$$\mathbf{u} = \begin{pmatrix} u \\ w \\ b \\ P \end{pmatrix}, \quad \mathbf{f}(\mathbf{u}) = \begin{pmatrix} -U \frac{\partial u}{\partial x} \\ -U \frac{\partial w}{\partial x} + b \\ -U \frac{\partial b}{\partial x} - N^2 w \\ -U \frac{\partial P}{\partial x} \end{pmatrix}, \quad L\mathbf{u} = \begin{pmatrix} -\frac{\partial P}{\partial x} \\ -\frac{\partial P}{\partial z} \\ 0 \\ -c_s^2 \left(\frac{\partial u}{\partial x} + \frac{\partial w}{\partial z} \right) \end{pmatrix}. \quad (29)$$

352 Having linearized the governing equations, $\mathbf{f}(\mathbf{u})$ is no longer a nonlinear function of \mathbf{u} , and
 353 we will alternatively write this term as $M\mathbf{u}$.

354 If (29) is integrated using the AI2*/AB3 method, the temporally discretized system
 355 becomes

$$P_3 \mathbf{u}^{n+1} + P_2 \mathbf{u}^n + P_1 \mathbf{u}^{n-1} + P_0 \mathbf{u}^{n-2} = \mathbf{0}, \quad (30)$$

356 where each of the P_n are 4x4 matrices, with $P_3 = I - \frac{5}{4}L\Delta t$, $P_2 = -I - \frac{23}{12}M\Delta t + L\Delta t$,
 357 $P_1 = \frac{4}{3}M\Delta t - \frac{3}{4}L\Delta t$ and $P_0 = -\frac{5}{12}M\Delta t$. The method (30) supports four physical modes (two
 358 sound-wave and two gravity-wave modes that are the discrete-in-time equivalents of (23))
 359 and eight computational modes, all of which are eigenvectors associated with the polynomial
 360 eigenvalue problem

$$(\lambda^3 P_3 + \lambda^2 P_2 + \lambda P_1 + P_0) \mathbf{u}^{n-2} = \mathbf{0}. \quad (31)$$

361 Note that equation (31) is the matrix analog of equation (16) with the amplification
 362 factor A replaced by the eigenvalue λ . Such polynomial eigenvalue problems can be solved
 363 in MATLAB using the command `polyeig` or, when P_3 is non-singular, by reformulating (31)
 364 as the standard eigenvalue problem $B\mathbf{v} = \lambda\mathbf{v}$ where

$$B = \begin{pmatrix} P_3^{-1}P_2 & P_3^{-1}P_1 & P_3^{-1}P_0 \\ I & 0 & 0 \\ 0 & I & 0 \end{pmatrix} \text{ and } \mathbf{v} = \begin{pmatrix} \mathbf{u}^n \\ \mathbf{u}^{n-1} \\ \mathbf{u}^{n-2} \end{pmatrix}. \quad (32)$$

365 The latter approach was taken for the computations in this paper.

366 Let Ψ be the maximum in absolute value of the eigenvalues arising from such a discrete-in-
 367 time IMEX approximation. Figure 7 shows Ψ for the T2 θ /LF⁸, AI2*/AB3 and BDF2/BX2*
 368 methods. Key values of Ψ are contoured as a function of Δt and the horizontal wavelength
 369 $\lambda_x = 2\pi/k$ for modes with fixed vertical wavelengths $\lambda_z = 2\pi/l$ of either 20 or 2 km.
 370 As apparent in Fig. 7, if Δt is increased, a mode with given (λ_x, λ_z) eventually exhibits
 371 spurious amplification, although the Δt at which this first occurs are not captured for all
 372 the horizontal wavelengths plotted in Fig. 7d,e. Also plotted as the solid line is the curve
 373 $F_1(\lambda_x, \Delta t) = C$, where $F_1 = (|2\pi U/\lambda_x| + N)\Delta t$ and C is 1.0, 0.72 or 0.67 for the T2 θ /LF,
 374 AI2*/AB3 and BDF2/BX2* methods, respectively. Note that $F_1(\lambda_x, \Delta t)$ is similar to the
 375 expression appearing in the stability condition (26) except that it is expressed in terms of
 376 the actual wavelength λ_x instead of the maximum resolved wavenumber k_{\max} . The curve
 377 $F_1(\lambda_x, \Delta t) = C$ divides the stable and unstable regions in the T2 θ /LF case, but lies within
 378 the stable region for the AI2*/AB3 and BDF2/BX2* cases.

The dashed curve in Fig. 7 shows the limit of the stability region for explicit LF, AB3
 or BX2* approximations to the highest-frequency gravity wave mode with horizontal and
 vertical wavelengths (λ_x, λ_z) , i.e., the dashed curve plots $F_2(\lambda_x, \Delta t) = C$, where $F_2(\lambda_x, \Delta t) =$
 $\omega_{\text{gD}}\Delta t$, ω_{gD} is the frequency determined by (25) for the downstream propagating mode, and
 C is 1.0, 0.72 or 0.67 in the respective T2 θ /LF, AI2*/AB3, and BDF2/BX2* cases. Since
 this curve matches the edge of the stable region in the AI2*/AB3 and BDF2/BX2* cases,
 both of these methods are stable whenever the associated explicit approximation (AB3 or
 BX2*) to the same gravity-wave mode would be stable. In contrast, the region of stability
 for the T2 θ /LF method is more restrictive than that for leapfrog approximations to the same
 gravity wave mode.⁹ The maximum stable time step for a mode of wavenumber k is reduced
 for the T2 θ /LF method relative to that for gravity waves of wavenumber k integrated with

⁸Throughout the following analysis of the T2 θ /LF scheme, we assume $\theta = 0.5$ and no time filtering.

⁹Of course completely explicit AB3 and leapfrog approximations to (18)–(21) would face more severe stability restrictions on Δt from the sound waves.

a fully explicit leapfrog scheme because the $2\Delta t$ -trapezoidal averaging in the implicit step replaces c_s in (24) with $\hat{c}_s = c_s \cos(\omega\Delta t)$. As $\omega\Delta t$ increases toward $\pi/2$ (a coarsely resolved $4\Delta t$ oscillation), the terms involving N^2/\hat{c}_s^2 begin to dominate the semi-discrete dispersion relation for the *sound-wave* modes. In the limit $\hat{c}_s \rightarrow 0$, that dispersion relation becomes

$$\left(\frac{\sin(\omega\Delta t)}{\Delta t} - Uk\right)^2 = \frac{\hat{c}_s^2}{2} \left(\frac{N^2}{\hat{c}_s^2} + \frac{N^2}{\hat{c}_s^2}\right) = N^2,$$

379 from which it follows that the condition $(Uk + N)\Delta t < 1$ is not only sufficient, but is also
 380 necessary for stability.

381 It is interesting that the implicitness introduced in the AI2*/AB3 and the BDF2/BX2
 382 schemes avoids the negative impact on the stability of individual gravity-wave modes, relative
 383 to the corresponding fully explicit approach, produced by the T2 θ /LF method. Nevertheless,
 384 the maximum Δt in any practical IMEX integration of (29) is limited by the numerically
 385 resolvable mode with the most severe stability constraint, and as apparent in Fig. 7, these
 386 are the modes with the shortest horizontal wavelengths. The maximum Δt is effectively
 387 limited by the stability condition (26), and the largest time step allowed by the AI2*/AB3
 388 (BDF2/BX2*) scheme is therefore smaller than that for the T2 θ /LF method by a factor of
 389 0.72 (0.67).

390 If the horizontal resolution is sufficiently coarse, $|Uk_{\max}| \ll N$ and (26) reduces to

$$N\Delta t < C, \tag{33}$$

391 in which case the time step is determined entirely by the Brunt-Väisälä frequency. In at-
 392 mospheric applications, the maximum N is $O(10^{-2}) \text{ s}^{-1}$ and the maximum stable time step
 393 dictated by (33) will be less than roughly 100 s. This time-step restriction can be relaxed by
 394 treating the terms labeled ‘b’ in (19) and (20) implicitly, in which case an IMEX splitting

395 of the form (1) becomes

$$\mathbf{f}(\mathbf{u}) = \begin{pmatrix} -U \frac{\partial u}{\partial x} \\ -U \frac{\partial w}{\partial x} \\ -U \frac{\partial b}{\partial x} \\ -U \frac{\partial P}{\partial x} \end{pmatrix}, \quad L\mathbf{u} = \begin{pmatrix} -\frac{\partial P}{\partial x} \\ -\frac{\partial P}{\partial z} + b \\ -N^2 w \\ -c_s^2 \left(\frac{\partial u}{\partial x} + \frac{\partial w}{\partial z} \right) \end{pmatrix}. \quad (34)$$

The implicit part of (34) includes all the terms responsible for gravity wave propagation in a resting fluid; if the vertical wavelength is sufficiently long, this propagation will be faster than that produced by typical atmospheric mean flows. Let us therefore denote the frequencies due to the gravity-wave propagation as $\tilde{\omega}_H$ and that due to advection as $\tilde{\omega}_L$, where for a specific mode

$$\tilde{\omega}_L = |Uk|, \quad \tilde{\omega}_H = \frac{N|k|}{(k^2 + l^2)^{1/2}}.$$

396 Figure 8 shows Ψ for T2 θ /LF, AI2*/AB3, BDF2/BX2* and BDF2/BX2 approximations
 397 to (34) contoured as a function of λ_x and Δt for the downstream moving gravity wave with a
 398 vertical wavelength of 20 km. Noting the difference in the scales on the vertical axis between
 399 Figs. 7 and 8, it is apparent that when λ_x is large, stable solutions to (34) can be obtained
 400 using much larger Δt than would be permitted when integrating the same mode using (29).
 401 To better appreciate the factors governing the stability of IMEX solutions to (34), two
 402 additional lines are plotted in Fig. 8. First consider the line $\tilde{\omega}_L \Delta t = C$ (dashed), where as
 403 before C is 1.0, 0.72 and 0.67 for the T2 θ /LF, AI2*/AB3, and BDF2/BX2* approximations,
 404 respectively.¹⁰ This line approximates the stability boundary for both schemes when the
 405 horizontal wavelength is short and the intrinsic frequency of the gravity waves are reduced
 406 by non-hydrostatic effects. These values are consistent with the values of $\omega_L \Delta t$ at which
 407 the stability boundary intersects the horizontal axis in Figs. 5a and 6d,e. Also consistent
 408 with Fig. 6b is the lack of a significant stable region for small horizontal wavelengths in the
 409 BDF2/BX2 case (Fig. 8d). Now consider the vertical line in each panel of Fig. 8, which is

¹⁰This line does not appear in Fig. 8d.

410 plotted at the value of λ_x for which $\tilde{\omega}_H/\tilde{\omega}_L = \xi$. The region to the right of this line is the
 411 region where the intrinsic frequency of the gravity waves exceeds that frequency produced
 412 by advection by a large enough factor to guarantee stability, independent of the value of Δt ,
 413 and consistent with Table 2, this is indeed the case.

414 4. A Nonlinear Test Case

The preceding theoretical analyses suggest new methods that may be an attractive candidates for IMEX approximations to the compressible equations of motion. In this section we evaluate the performance of several of these methods in a pair of nonlinear test cases involving two-dimensional (x - z) nonlinear gravity waves generated by a localized region of non-divergent forcing in a stratified shear flow. The background horizontal wind is

$$u_0(z) = 5 + z + 0.4(5 - z)(5 + z) \quad \text{m s}^{-1}$$

where z is the vertical coordinate in km. The waves are forced by the curl of a nondivergent streamfunction

$$\psi(x, z, t) = \psi_0 x \sin(\omega t) \exp \left[- \left(\frac{x}{L_x} \right)^2 - \left(\frac{z}{L_z} \right)^2 \right] \quad \text{m}^2 \text{ s}^{-1},$$

415 where x denotes the horizontal coordinate in km, and the values of ψ_0 , ω , L_x , and L_z for
 416 each case are listed in Table 3.

417 The first case, NH for which $\omega/N = 1/4$, is dominated by nonhydrostatic motions and
 418 employs a grid spacing representative of high-resolution convective cloud models (see Table 3
 419 for values of the numerical parameters). The dynamics in the second case, H for which
 420 $\omega/N = 6.25 \times 10^{-3}$, are quasi-hydrostatic and the grid spacing in this case is representative
 421 of a high-resolution global model. Empirical stability limits for the various methods are
 422 determined by integrating each scheme to a time t_d , chosen such that, at the coarsest time
 423 resolution, more than 8,500 time steps are required to reach t_d . In case NH, the waves

424 generated by the forcing break in very localized regions and gradually accelerate the mean
 425 flow. To keep the effective CFL number constant during the long-time NH integrations, the
 426 horizontally-averaged mean flow \bar{u} is gradually relaxed back towards its initial shear profile
 427 over a timescale $\tau = 3000$ s. No relaxation is used in case H.

428 This problem is governed by the system

$$\frac{Du}{Dt} + \frac{\partial P}{\partial x} = -\frac{\partial \psi}{\partial z} + \frac{u_0(z) - \bar{u}(z, t)}{\tau}, \quad (35)$$

$$\frac{Dw}{Dt} + \frac{\partial P}{\partial z} = b + \frac{\partial \psi}{\partial x}, \quad (36)$$

$$\frac{Db}{Dt} + N^2 w = 0, \quad (37)$$

$$\frac{DP}{Dt} + c_s^2 \left(\frac{\partial u}{\partial x} + \frac{\partial w}{\partial z} \right) = 0, \quad (38)$$

where

$$\frac{D}{Dt} = \frac{\partial}{\partial t} + u \frac{\partial}{\partial x} + w \frac{\partial}{\partial z},$$

429 $N = 0.02 \text{ s}^{-1}$ and $c_s = 350 \text{ m s}^{-1}$.

We will investigate convergence in the time domain while keeping the spatial discretiza-
 tion fixed. In all simulations the numerical domain is horizontally periodic and bounded
 by flat rigid upper and lower surfaces. Let m and n be integer indices; the mesh is stag-
 gered so that the equation for P applies at points $(m\Delta x, n\Delta y)$, that for u applies at points
 $((m - \frac{1}{2})\Delta x, n\Delta z)$, and those for b and w at points $(m\Delta x, (n - \frac{1}{2})\Delta z)$. Using the operator
 notation

$$\delta_{nx} f(x) = \frac{f(x + n\Delta x/2) - f(x - n\Delta x/2)}{n\Delta x}, \quad \langle f(x) \rangle^{nx} = \frac{f(x + n\Delta x/2) + f(x - n\Delta x/2)}{2},$$

430 the spatial finite differencing has the form

$$\frac{\partial u}{\partial t} + \frac{1}{2} \delta_{2x}(u^2) + \langle \langle w \rangle^x \delta_z u \rangle^z + \delta_x P = \frac{u_0(z) - \bar{u}(z, t)}{\tau} - K ((\Delta x \delta_x)^2 + (\Delta z \delta_z)^2) u, \quad (39)$$

$$431 \quad \frac{\partial w}{\partial t} + \langle \langle u \rangle^z \delta_x w \rangle^x + \frac{1}{2} \delta_{2z}(w^2) + \delta_z P - b = -K ((\Delta x \delta_x)^2 + (\Delta z \delta_z)^2) w, \quad (40)$$

$$432 \quad \frac{\partial b}{\partial t} + \langle \langle u \rangle^z \delta_x b \rangle^x + \langle \langle w \rangle^z \delta_z b \rangle^z + N^2 w = -K ((\Delta x \delta_x)^2 + (\Delta z \delta_z)^2) b, \quad (41)$$

$$\frac{\partial P}{\partial t} + \langle u \delta_x P \rangle^x + \langle w \delta_z P \rangle^z + c_s^2 (\delta_x u + \delta_z w) = 0, \quad (42)$$

434 where nonlinear instability is prevented and a simple parameterization of turbulent mixing
 435 in a nearly inviscid fluid is imposed through the fourth-derivative hyper-diffusion terms with
 436 the values of K listed in Table 3. The pressure field for the T2 θ /LF scheme is updated
 437 solving a Helmholtz equation for pressure in the manner described in Durran (2010, Section
 438 8.2.5). The pressure equations arising for the other methods are solved in a similar manner.
 439 To stabilize the explicit step in the T2 θ /LF scheme, the terms on the right side of (39)–(41)
 440 are integrated using a forward time step over the interval $2\Delta t$. This low-accuracy forward
 441 step is neither required nor used with the other IMEX schemes. The starting stages (one
 442 or two in the case of two-step and three-step methods, respectively) are computed using the
 443 third-order IMEX additive Runge-Kutta method of Kennedy and Carpenter (2003).

444 Figure 9 shows contours of the u field at time t_d in a central portion of the full domain
 445 for the reference solution for cases NH and H. Also shown by gray shading are contours of
 446 the ψ field. The reference solution was computed with a fully explicit fourth-order Runge-
 447 Kutta scheme using a very short time step. The time t_d is well before the moment when
 448 the evolving gravity waves begin to wrap around the domain through the periodic lateral
 449 boundaries. It is perhaps counter-intuitive that the forcing projects most strongly onto the
 450 upstream propagating mode in case H, but this was easy to verify analytically in a separate
 451 constant-wind-speed simulation with $u_0 = 8 \text{ m s}^{-1}$ (not shown).

452 The accuracy of these semi-implicit methods for case NH is compared in Fig. 10, which
 453 shows the relative error in b plotted on a log-log scale as a function of the Courant number
 454 associated with horizontal advection, $\max_{x,z} u(t_d) \Delta t / \Delta x$. The relative error is evaluated as
 455 the RMS difference between the b field at $t = t_d$ computed by each semi-implicit method
 456 and the result obtained from the reference solution b_r , normalized by the RMS value of b_r .

457 Results for schemes that have seen previous use are given in Fig. 10a. At all but the
 458 smallest CFL number (which may be of little practical importance) the best results are

459 obtained using the T2 θ /LF with the RAW filter and no off-centering of the trapezoidal time
 460 difference, i.e., $(\theta, \gamma, \sigma) = (0.5, 0.2, 0.53)$. The worst accuracy is obtained using RA filtering
 461 and the T2 θ /LF method with $\theta = 0.6$ while implicitly updating the buoyancy-forcing terms,
 462 which are the terms in (40) and (41) that are identical to the those labeled “b” in (19)
 463 and (20). Setting $\theta = 0.5$ reduces the error, but still yields a first-order scheme due to
 464 the influence of the RA filter. When $\theta = 0.5$, treating the buoyancy explicitly instead of
 465 implicitly with the T2 θ /LF-RA method has no impact on accuracy (compare the diamonds
 466 and the solid black line), but if $\theta = 0.6$, switching from implicit to explicit differencing for the
 467 buoyancy reduces the error to almost the same values obtained when $\theta = 0.5$ (compare the
 468 \times 's and the dot-dashed black line). Evidently, off-centering the trapezoidal time differencing
 469 degrades accuracy much more than the use of the RA filter. Finally, unlike the first-order
 470 time-filtered T2 θ /LF-methods, the BDF2/BX2 scheme exhibits second-order convergence,
 471 but it does not actually yield more accurate results than the T2 θ /LF-RAW method unless
 472 the advective CFL number is very small.

473 Fig. 10b shows the performance of the new methods. At a given time step, the smallest
 474 errors are produced when buoyancy is treated explicitly using AI2*/AB3 or BI2*/BX3*,
 475 both of which feature third-order accurate explicit schemes. In fact, the overall convergence
 476 rate for these two methods appears to be third-order, which is surprising since even when
 477 the buoyancy is explicit, the pressure gradient and divergence terms are still integrated using
 478 second-order implicit schemes. At the same advective CFL number of 0.57, the T2 θ /LF-
 479 RAW scheme, which is the best leapfrog-trapezoidal method, generates roughly four times
 480 the error of the AI2*/AB3 method, and this difference increases rapidly as the time step is
 481 further reduced. If the buoyancy is treated implicitly, all the new schemes behave similarly,
 482 but the best are BDF2/BX2* and AM2*/AX2* which use superior implicit schemes. Again,
 483 these new schemes deliver more accuracy at a given time step (advective CFL number) than
 484 those shown in Fig. 10a, although when the buoyancy is implicit, they are only slightly

485 superior to the T2 θ /LF-RAW method at the largest CFL numbers.

486 Each of the curves shown in Fig. 10 terminates at the largest value of $\max_{x,z}(u(t_d))\Delta t/\Delta x$
487 for which the solutions could be integrated to t_f without any sign of incipient instability. These
488 empirically determined stability limits are listed in Table 4 to within an accuracy to ± 0.01 .
489 In case NH, the largest stable time step is permitted by the RAW-filtered T2 θ /LF method
490 with buoyancy treated implicitly. The maximum stable advective CFL numbers permitted
491 by the new Adams and backward IMEX methods are smaller than that for the RAW-filtered
492 T2 θ /LF method by a factor of about 0.8. The BDF2/BX2 scheme requires much smaller
493 time steps than any of the other methods.

494 Fig. 11 gives the same information as Fig. 10 for case H. In case H, the basic behaviors
495 of all the methods remain similar to those discussed in case NH, although the gravity waves
496 travel much faster. As a consequence, the maximum advective CFL number for which stable
497 integrations can be performed when the buoyancy is explicit is roughly 1/5 of that which
498 can be used in case NH (recall the logarithmic scaling of the axes in these plots, and see also
499 Table 4). It is therefore, not likely practical to treat the buoyancy explicitly in problems
500 similar to case H. When buoyancy is implicit, the magnitude of the high-frequency (gravity
501 wave) forcing over the low frequency (advective) forcing is greater in case H than in case NH,
502 and therefore the maximum stable CFL numbers in case H are larger than those in case NH
503 (consistent with the stability regions in Figs. 5 and 6). The largest advective CFL number is
504 again permitted by the RAW-filtered T2 θ /LF method, but that for the AM2*/AX2* method
505 is only smaller by a factor of 0.96. Note also, that when buoyancy is treated implicitly, the
506 superiority of the new Adams and backward schemes with good implicit parts (AM2*/AX2*
507 and BDF2/BX2*) over their cousins with explicit third-order parts is more pronounced than
508 in case NH.

5. Discussion and Conclusions

We have proposed two new families of IMEX multistep methods for the efficient solution of fast-wave, slow-wave problems in which the fast waves need not be accurately simulated. One family is based on Adams methods, the other on backward differencing schemes. In both cases the implicit parts of the schemes are two-step second-order A -stable methods. The explicit parts are second-order three-step methods, except for two that are third-order. We focused on four members of these two families, the two with nominally the best implicit schemes: AM2*/AX2* and BDF2/BX2*, and the two with third-order explicit parts: AI2*/AB3 and BI2*/BX3*.

These new schemes were compared against previously proposed versions of the IMEX leapfrog-trapezoidal method and the BDF2/BX2 scheme in three contexts: the oscillation equation with separate high- and low-frequency forcing, and both the linearized and the non-linear “compressible Boussinesq” system. When it is practical to approximate the buoyancy forcing terms with the explicit part of the IMEX scheme, AI2*/AB3 and BI2*/BX3* appear to give considerably more accurate results than the other methods, while still permitting time steps with advective CFL numbers only slightly smaller than the best leapfrog-trapezoidal scheme. When buoyancy is implicit, the improvement obtained using the best new schemes (which in the case with implicit buoyancy are AM2*/AX2* and BDF2/BX2*) is less pronounced; in particular, the RAW filtered leapfrog-trapezoidal method performed almost as well and allowed a slightly larger time step.

One additional advantage of the new methods is that the explicit parts of these schemes are capable of naturally approximating terms arising from dissipation or model physics, whereas such terms must be incorporated in the explicit part of leapfrog-trapezoidal methods using a first-order Euler step over a time interval of $2\Delta t$. Finally, we note that off-centering the trapezoidal update in the T2 θ /LF method with $\theta = 0.6$ gave very inaccurate results in both cases H and NH. The damping produced by such off-centering is not very scale selective,

535 and the numerical results for this scheme were notably worse than all the others.

536 The stability constraints for the previously used BDF2/BX2 method require a much
537 smaller advective CFL number than that for the other schemes. In the context considered
538 here, in which periodic horizontal boundary conditions allow the implicit problem to be
539 solved efficiently using direct methods, this constraint on the time step is a serious disad-
540 vantage. On the other hand, in those circumstances where iterative solvers are employed,
541 the overall efficiency of the method depends on the condition number of the coefficient ma-
542 trix arising from the implicit part of the scheme. When buoyancy is treated explicitly, the
543 condition number for the implicit sub-problem in our nonlinear test case is very closely
544 proportional to

$$\left(\frac{\nu_1}{\alpha_1}\right)^2 \frac{(c_s \Delta t)^2}{(\Delta x)^2 + (\Delta z)^2} \quad (43)$$

545 where α_1 and ν_1 are the coefficients of the state variables at the new time level listed for
546 each scheme in Table 1. The condition number is influenced by both the implicit part of
547 the IMEX scheme and by the time-step. Giraldo (2005) noted that, provided the condition
548 number is small enough to dramatically reduce the number of iterations required during
549 each implicit step, the most efficient scheme can sometimes be one for which ν_1/α_1 and the
550 maximum time step are both small.

551 The values of $(\nu_1/\alpha_1)^2$ for the preceding implicit methods are listed in Table 5. The
552 smallest value is associated with the modified Crank-Nicolson scheme MCN of Ascher et al.
553 (1995). The member of the family of stable IMEX Adams schemes for fast-wave/slow-wave
554 problems that uses the MCN scheme is listed in Table 1. Among the two-step second-
555 order implicit Adams methods, MCN has the best damping properties at negative infinity
556 ($|A| \rightarrow 1/3$ as $\Re\{\eta\} \rightarrow -\infty$ in (3)), but its fast-wave/slow-wave stability properties are worse
557 than the schemes created using BDF2 and AM2*, so we have not focused on this method.
558 In problems where the condition number is of primary concern, however, this method might
559 be attractive.

560 Among the other methods, BDF2 has the next smallest condition number, followed by
561 AM2*. AI2* has the largest condition number, and is the only one of the newly proposed
562 schemes with a condition number larger than the T2 θ schemes. When the condition number
563 is a significant consideration, BI2*/BX3* would be a much better choice than AI2*/AB3 for
564 an IMEX scheme with a third-order explicit step.

565 In this paper we have endeavored to investigate a large class of IMEX linear multistep
566 methods. Linear multistep methods are one of the most important families of methods for
567 the solution of ordinary differential equations, but they are not the only approach. Another
568 very important approach involves multistage methods, the most prominent of which are
569 Runge-Kutta schemes, and IMEX Runge-Kutta schemes have been used in many advection-
570 diffusion problems. An investigation of IMEX Runge-Kutta schemes for the fast-wave/slow-
571 wave problem is beyond the scope of this paper, but has recently been discussed by Ullrich
572 and Jablonowski (2011).

573 *Acknowledgments.*

574 The authors benefited from discussions with Frank Giraldo and from comments by the
575 anonymous reviewers. This research was supported by the National Science Foundation
576 through grant ATM-0836316 and the Office of Naval Research through contract number
577 N00173-10-1-G033.

REFERENCES

- 580 Ascher, U. M., S. J. Ruuth, and B. T. R. Wetton, 1995: Implicit-explicit methods for time-
581 dependent partial differential equations. *SIAM J. Numer. Anal.*, **32**, 797–823.
- 582 Asselin, R., 1972: Frequency filter for time integrations. *Mon. Wea. Rev.*, **100**, 487–490.
- 583 Bannon, P. R., 1996: On the anelastic approximation for a compressible atmosphere. *J.*
584 *Atmos. Sci.*, **53**, 3618–3628.
- 585 Benoit, R., M. Desgagné, P. Pellerin, S. Pellerin, Y. Chartier, and S. Desjardins, 1997: The
586 Canadian MC2: A semi-Lagrangian, semi-implicit wideband atmospheric model suited for
587 finescale process studies and simulation. *Mon. Wea. Rev.*, **125**, 2382–2415.
- 588 Dahlquist, G. G., 1963: A special stability problem for linear multistep methods. *BIT*, **3**,
589 27–43.
- 590 Durran, D. R., 1989: Improving the anelastic approximation. *J. Atmos. Sci.*, **46**, 1453–1461.
- 591 Durran, D. R., 1991: The third-order Adams-Bashforth method: An attractive alternative
592 to leapfrog time differencing. *Mon. Wea. Rev.*, **119**, 702–720.
- 593 Durran, D. R., 2008: A physically motivated approach for filtering acoustic waves from the
594 equations governing compressible stratified flow. *J. Fluid Mech.*, **601**, 365–379.
- 595 Durran, D. R., 2010: *Numerical Methods for Fluid Dynamics: with Applications in Geo-*
596 *physics*. Springer, New York, 516 p.
- 597 Evans, K. J., M. A. Taylor, and J. B. Drake, 2010: Accuracy analysis of a spectral element
598 atmospheric model using a fully implicit solution framework. *Mon. Wea. Rev.*, **138**, 3333–
599 3341.

- 600 Fornberg, B. and T. A. Driscoll, 1999: A fast spectral algorithm for nonlinear wave equations
601 with linear dispersion. *J. Comp. Phys.*, **155**, 456–467.
- 602 Frank, J., W. Hundsdorfer, and J. G. Verwer, 1997: On the stability of implicit-explicit
603 linear multistep methods. *Applied Numer. Math.*, **25**, 193–205.
- 604 Giraldo, F., M. Restelli, and M. Läuter, 2010: Semi-implicit formulations of the Navier–
605 Stokes equations: Application to nonhydrostatic atmospheric modeling. *SIAM J. Sci.*
606 *Comput.*, **32**, 3394–3425.
- 607 Giraldo, F. X., 2005: Semi-implicit time-integrators for a scalable spectral element atmo-
608 spheric model. *Q.J.R. Meteorol. Soc.*, **131**, 2431–2454, doi:10.1256/qj.03.218.
- 609 Karniadakis, G. E., M. Israeli, and S. A. Orszag, 1991: High-order splitting methods for the
610 incompressible Navier-Stokes equations. *J. Comp. Phys.*, **97**, 414–443.
- 611 Kennedy, C. A. and M. H. Carpenter, 2003: Additive Runge-Kutta schemes for
612 convection-diffusion-reaction equations. *Appl. Numer. Math.*, **44**, 139–181, doi:doi:10.
613 1016/S0168-9274(02)00138-1.
- 614 Klemp, J. B. and R. Wilhelmson, 1978: The simulation of three-dimensional convective
615 storm dynamics. *J. Atmos. Sci.*, **35**, 1070–1096.
- 616 Kwizak, M. and A. J. Robert, 1971: A semi-implicit scheme for grid point atmospheric
617 models of the primitive equation. *Mon. Wea. Rev.*, **99**, 32–36.
- 618 Lipps, F. and R. Hemler, 1982: A scale analysis of deep moist convection and some related
619 numerical calculations. *J. Atmos. Sci.*, **39**, 2192–2210.
- 620 Nevanlinna, O. and W. Liniger, 1978: Contractive methods for stiff differential equations
621 part I. *BIT*, **18**, 457–474.

- 622 Ogura, Y. and N. A. Phillips, 1962: Scale analysis for deep and shallow convection in the
623 atmosphere. *J. Atmos. Sci.*, **19**, 173–179.
- 624 Robert, A. J., 1966: The integration of a low order spectral form of the primitive meteorolo-
625 gical equations. *J. Meteor. Soc. Japan*, **44**, 237–244.
- 626 Tapp, M. C. and P. W. White, 1976: A non-hydrostatic mesoscale model. *Q. J. R. Meteorol.*
627 *Soc.*, **102**, 277–296.
- 628 Tatsumi, Y., 1983: An economical explicit time integration scheme for a primitive model. *J.*
629 *Meteor. Soc. Japan*, **61**, 269–287.
- 630 Ullrich, P. and C. Jablonowski, 2011: Operator-split Runge-Kutta-Rosenbrock (RKR)
631 methods for non-hydrostatic models. *Mon. Wea. Rev.*, in press, doi:10.1175/MWR-D-
632 10-05073.1.
- 633 Varah, J. M., 1980: Stability restrictions on second order, three level finite difference schemes
634 for parabolic equations. *SIAM J. Numer. Analysis*, **17**, 300–309.
- 635 Wicker, L. J. and W. C. Skamarock, 2002: Time-splitting methods for elastic models using
636 forward time schemes. *Mon. Wea. Rev.*, **130**, 2088–2097.
- 637 Williams, P. D., 2009: A proposed modification to the Robert–Asselin time filter. *Mon. Wea.*
638 *Rev.*, **137**, 2538–2546.
- 639 Williams, P. D., 2011: The RAW filter: An improvement to the Robert–Asselin filter in
640 semi-implicit integrations. *Mon. Wea. Rev.*, **139**, 1996–2007.

641 List of Tables

- 642 1 Coefficients of implicit-explicit multistep methods following equation (2). In
643 the first column, values of c are given for implicit Adams (5) and backward
644 (6) methods. The values of b are listed for explicit Adams (10) and backward
645 (11) schemes. 33
- 646 2 Parameters characterizing regions of stability for solutions to (12) using the
647 the implicit-explicit multistep methods listed in Table 1. Values for the
648 leapfrog-Robert-Asselin scheme (LF-RA) were computed using $\gamma = 0.2$, $\sigma = 1$,
649 while for the leapfrog-Robert-Asselin-Williams (LF-RAW) variant, $\gamma = 0.2$,
650 $\sigma = 0.53$. 34
- 651 3 Physical and numerical parameters for the nonlinear simulations. 35
- 652 4 Maximum advective CFL numbers at which each method remains stable. “Ex-
653 plicit” and “Implicit” refer to the treatment of the buoyancy forcing in (40)
654 and (41), which are identical to the terms labeled “b” in (19) and (20). The
655 triplet of numbers after the T2 θ /LF methods denote the values of (θ, γ, σ) .
656 Values are empirically determined to within ± 0.01 36
- 657 5 Influence of the implicit scheme the condition number in the explicit-buoyancy
658 test problem. 37

TABLE 1. Coefficients of implicit-explicit multistep methods following equation (2). In the first column, values of c are given for implicit Adams (5) and backward (6) methods. The values of b are listed for explicit Adams (10) and backward (11) schemes.

Method		α_1	α_0	α_{-1}	β_0	β_{-1}	β_{-2}	ν_1	ν_0	ν_{-1}
Implicit	Explicit									
T2 θ	LF	1/2	0	-1/2	1	0	0	θ	0	1- θ
T1	AB3	1	-1	0	23/12	-4/3	5/12	1/2	1/2	0
MCN ($c=1/8$)	AX2+ ($b=3/8$)	1	-1	0	27/16	-7/8	3/16	9/16	3/8	1/16
AM2* ($c=1/2$)	AX2* ($b=1/2$)	1	-1	0	7/4	-1	1/4	3/4	0	1/4
AI2* ($c=3/2$)	AB3 ($b=5/6$)	1	-1	0	23/12	-4/3	5/12	5/4	-1	3/4
BDF2 ($c=0$)	BX2 ($b=0$)	3/2	-2	1/2	2	-1	0	1	0	0
BDF2 ($c=0$)	BX2* ($b=1/2$)	3/2	-2	1/2	5/2	-2	1/2	1	0	0
BI2* ($c=1/3$)	BX3* ($b=2/3$)	3/2	-2	1/2	8/3	-7/3	2/3	4/3	-2/3	1/3

TABLE 2. Parameters characterizing regions of stability for solutions to (12) using the the implicit-explicit multistep methods listed in Table 1. Values for the leapfrog-Robert-Asselin scheme (LF-RA) were computed using $\gamma = 0.2$, $\sigma = 1$, while for the leapfrog-Robert-Asselin-Williams (LF-RAW) variant, $\gamma = 0.2$, $\sigma = 0.53$.

Method		θ	μ	ξ
Implicit	Explicit			
T2 θ	LF	0.5	1	1
T2 θ	LF	0.6	0	1
T2 θ	LF-RA	0.5	0.91	1.22
T2 θ	LF -RA	0.6	0	1.17
T2 θ	LF-RAW	0.5	0.43	1.02
T2 θ	LF-RAW	0.6	0	1
T1	AB3	-	0	∞
AM2*	AX2*	-	0.76	3
AI2*	AB3	-	0.72	1.23
BDF2	BX2	-	0	3
BDF2	BX2*	-	0.67	5
BI2*	BX3*	-	0.72	2.43

TABLE 3. Physical and numerical parameters for the nonlinear simulations.

Parameter	Case NH	Case H
<i>Physical parameters</i>		
ω (s ⁻¹)	0.005	1.25×10^{-4}
L_x (km)	20	160
L_z (km)	5	10
ψ_0 (m ² s ⁻¹)	4	10
<i>Numerical parameters</i>		
Domain width (km)	300	12,000
Domain depth (km)	10	10
Δx (km)	0.25	10
Δz (m)	50	250
K (s ⁻¹)	3×10^{-2}	7.5×10^{-4}
Diagnosis time t_d (s)	3000	1.2×10^5
End time t_f (s)	10^5	4×10^6

TABLE 4. Maximum advective CFL numbers at which each method remains stable. “Explicit” and “Implicit” refer to the treatment of the buoyancy forcing in (40) and (41), which are identical to the terms labeled “b” in (19) and (20). The triplet of numbers after the T2 θ /LF methods denote the values of (θ, γ, σ) . Values are empirically determined to within ± 0.01

Method	Case NH		Case H	
	Explicit	Implicit	Explicit	Implicit
BDF2/BX2	0.26	0.30	0.03	0.22
T2 θ /LF (0.5,0.2,1)	0.66	0.69	0.08	0.75
T2 θ /LF (0.6,0.2,1)	0.66	0.62	0.13	0.75
T2 θ /LF (0.5,0.2,0.53)	0.73	0.73	0.08	0.78
AM2*/AX2*	0.60	0.61	0.13	0.75
AI2*/AB3	0.57	0.59	0.11	0.70
BDF2/BX2*	0.57	0.59	0.11	0.66
BI2*/BX3*	0.58	0.59	0.11	0.72

TABLE 5. Influence of the implicit scheme the condition number in the explicit-buoyancy test problem.

Method	$(\alpha_1/\nu_1)^2$
MCN	0.316
BDF2	0.444
AM2*	0.562
BI2*	0.790
T2 θ , $\theta = 0.5$	1.00
T2 θ , $\theta = 0.6$	1.44
AI2*	1.56

659 List of Figures

- 660 1 The magnitude of the amplification factor $|A|$ for several implicit approxima-
661 tions to the test problem (3), plotted as a function of the real and imaginary
662 parts of $\eta\Delta t$. Also shown, by the thin solid contours, is the magnitude of the
663 amplification factor for the exact solution. The labels for each panel corre-
664 spond to the terminology in the text and Table 1. The number in the lower
665 left of each panel is the limit of $|A|$ as $\Re\{\eta\} \rightarrow -\infty$ 41
- 666 2 Magnitude of the amplification factor (a) and the relative phase error (b) of
667 the schemes used for the implicit part of the IMEX formulae in Table 1. 42
- 668 3 As in Fig. 1 for the explicit part of the IMEX formulae in Table 1. 43
- 669 4 Magnitude of the amplification factor (a) and relative phase error (c) for the
670 physical modes of the schemes used for the explicit part of the IMEX formulae
671 in Table 1. Magnitudes of the amplification factors for the computational
672 modes are shown in (b). 44
- 673 5 Magnitude of the amplification factor for the leapfrog-based IMEX schemes
674 listed in Table 1 for the model problem (12). The contour interval is 0.1,
675 except that regions with $1 < |A| < 1.01$ are shaded gray and regions in which
676 $|A|$ exceeds 1.01 are shaded dark gray. Only the upper half-plane is plotted,
677 the values of $|A|$ in the lower half plane are anti-symmetric about the origin. 45
- 678 6 As in Fig. 5 except for the Adams and the backward-differenced IMEX schemes
679 listed in Table 1. 46

- 680 7 Stable regions as determined from the maximum eigenvalue Ψ for wave solu-
681 tions to the compressible Boussinesq equations using the IMEX decomposition
682 (29). Ψ is contoured as function of horizontal wavelength and time step for
683 modes with vertical wavelengths of 20 km (top row) and 2 km, bottom row.
684 Values for the T2 θ /LF method are shown in the left column; those for the
685 AI2*/AB3 method appear on the right. Regions with $0 \leq \Psi \leq 1$ are white,
686 those with $1 < \Psi < 1.01$ are light gray and regions in which Ψ exceeds 1.01
687 are dark gray. Also plotted are the curves for $F_1(\lambda_x, \Delta t) = C$ (solid line) and
688 $F_2(\lambda_x, \Delta t) = C$ (dashed); see text. 47
- 689 8 Contours of Ψ indicating stable regions as in the first row of Fig. 7, except for
690 the IMEX decomposition (34), and the addition of the BDF2/BX2 method in
691 panel (d). Shading conventions are as in Fig. 7. Note the horizontal scale in
692 panels (c) and (d) is almost double that in (a) and (b). Also shown are the
693 lines $\tilde{\omega}_L \Delta t = C$ (dashed) and $\tilde{\omega}_H / \tilde{\omega}_L = \xi$ (solid). 48
- 694 9 Contours of the horizontal velocity at $t = t_d$ in the central portion of the
695 domain for (a) case NH and (b) case H. Gray shades show contours of ψ with
696 steps in the gray scale at ± 5 and $\pm 15 \text{ m}^2 \text{ s}^{-2}$ in case NH and $\pm 1 \text{ m}^2 \text{ s}^{-2}$ in
697 case H. 49

698	10	Log-log plot of the error in the buoyancy field as a function of advective	
699		Courant number for the several of the methods listed in Table 1 for case NH.	
700		The curves show the result when buoyancy is treated implicitly; the symbols	
701		show the results when the buoyancy terms are approximated using the explicit	
702		part of the scheme. The lines/symbols terminate at the largest advective CFL	
703		number for which each method is stable. Thin dashed lines show the slopes	
704		corresponding to first, second and third-order convergence. The triplet of	
705		numbers after the T2 θ /LF methods denote the values of (θ, γ, σ) .	50
706	11	As in Fig. 10 for case H.	51

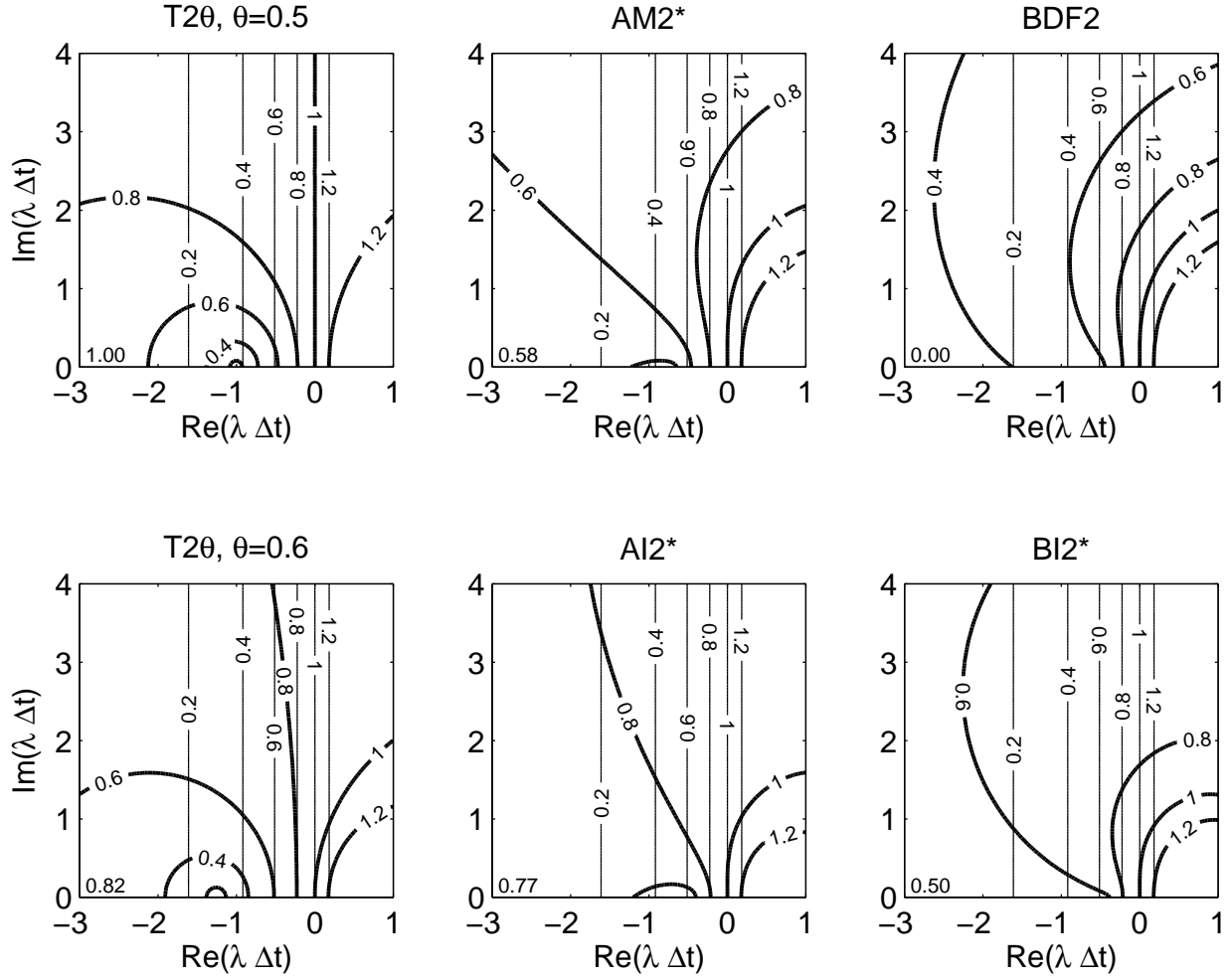


FIG. 1. The magnitude of the amplification factor $|A|$ for several implicit approximations to the test problem (3), plotted as a function of the real and imaginary parts of $\eta\Delta t$. Also shown, by the thin solid contours, is the magnitude of the amplification factor for the exact solution. The labels for each panel correspond to the terminology in the text and Table 1. The number in the lower left of each panel is the limit of $|A|$ as $\Re\{\eta\} \rightarrow -\infty$

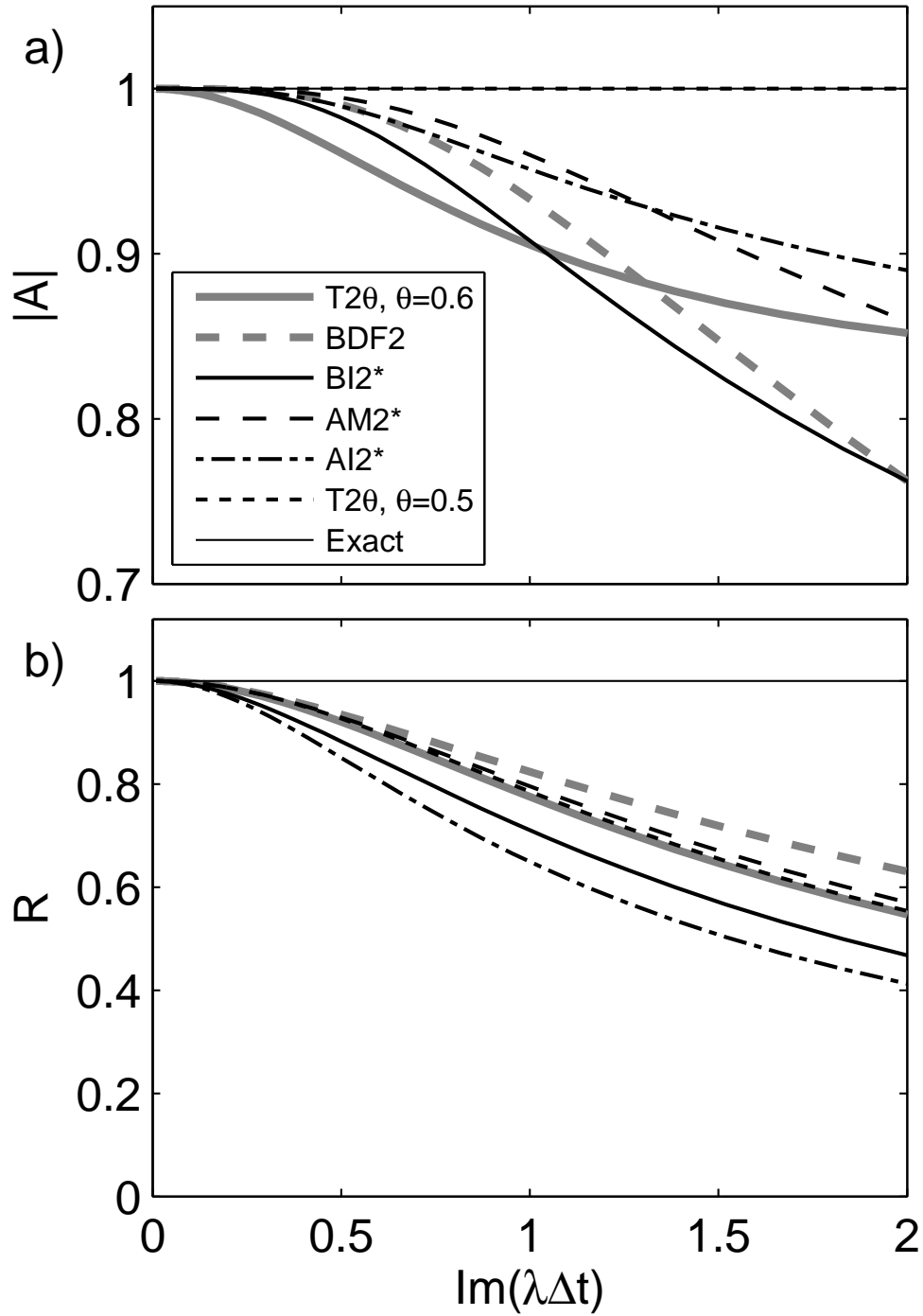


FIG. 2. Magnitude of the amplification factor (a) and the relative phase error (b) of the schemes used for the implicit part of the IMEX formulae in Table 1.

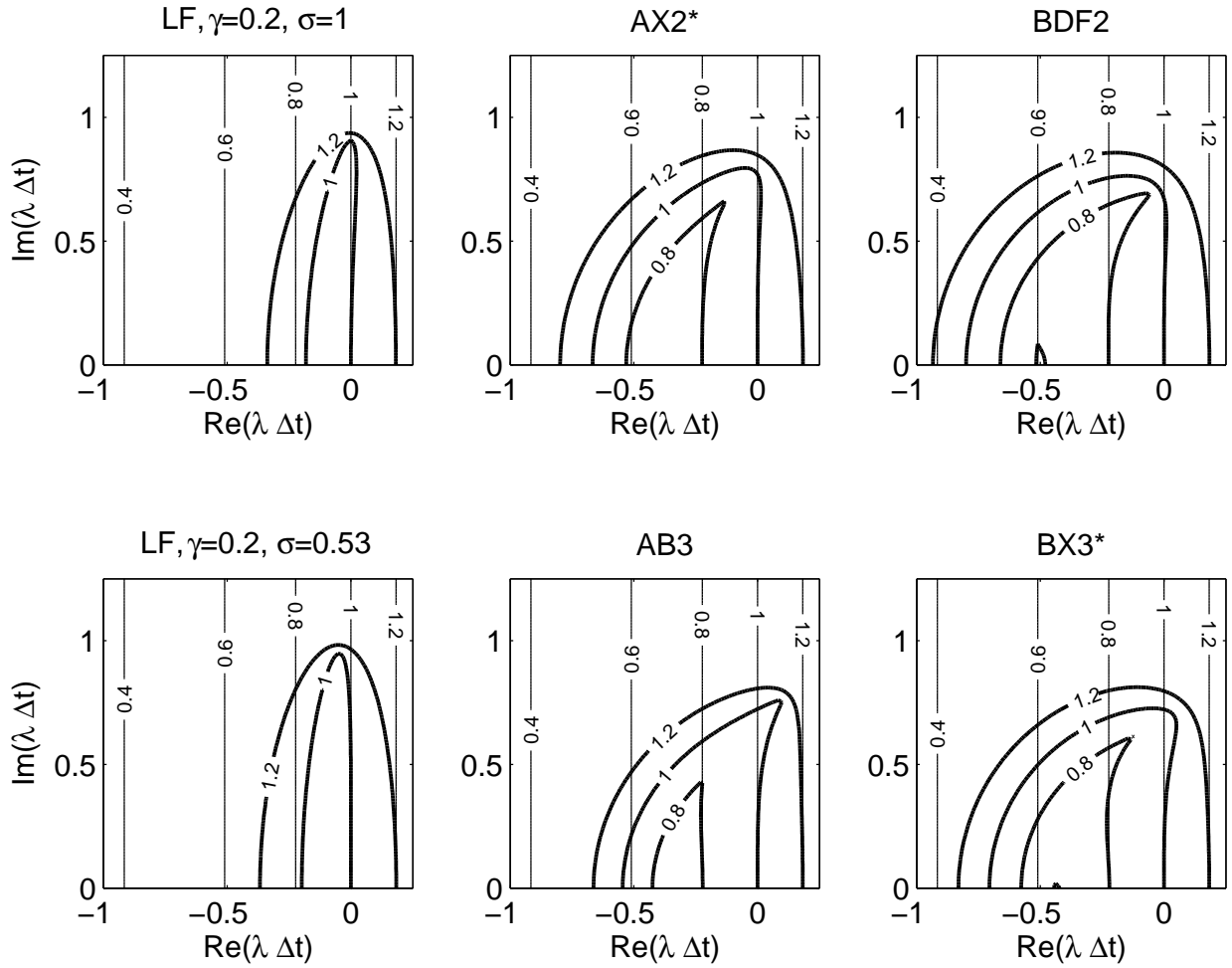


FIG. 3. As in Fig. 1 for the explicit part of the IMEX formulae in Table 1.

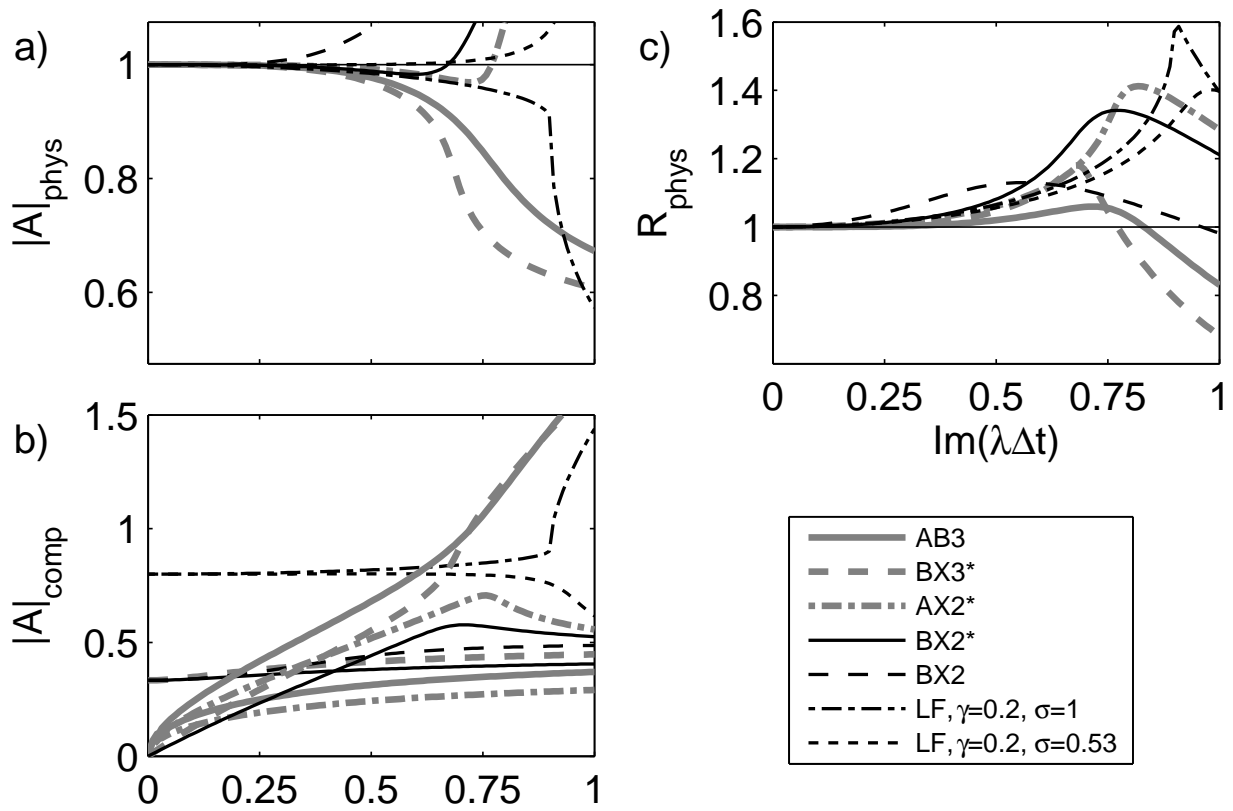


FIG. 4. Magnitude of the amplification factor (a) and relative phase error (c) for the physical modes of the schemes used for the explicit part of the IMEX formulae in Table 1. Magnitudes of the amplification factors for the computational modes are shown in (b).

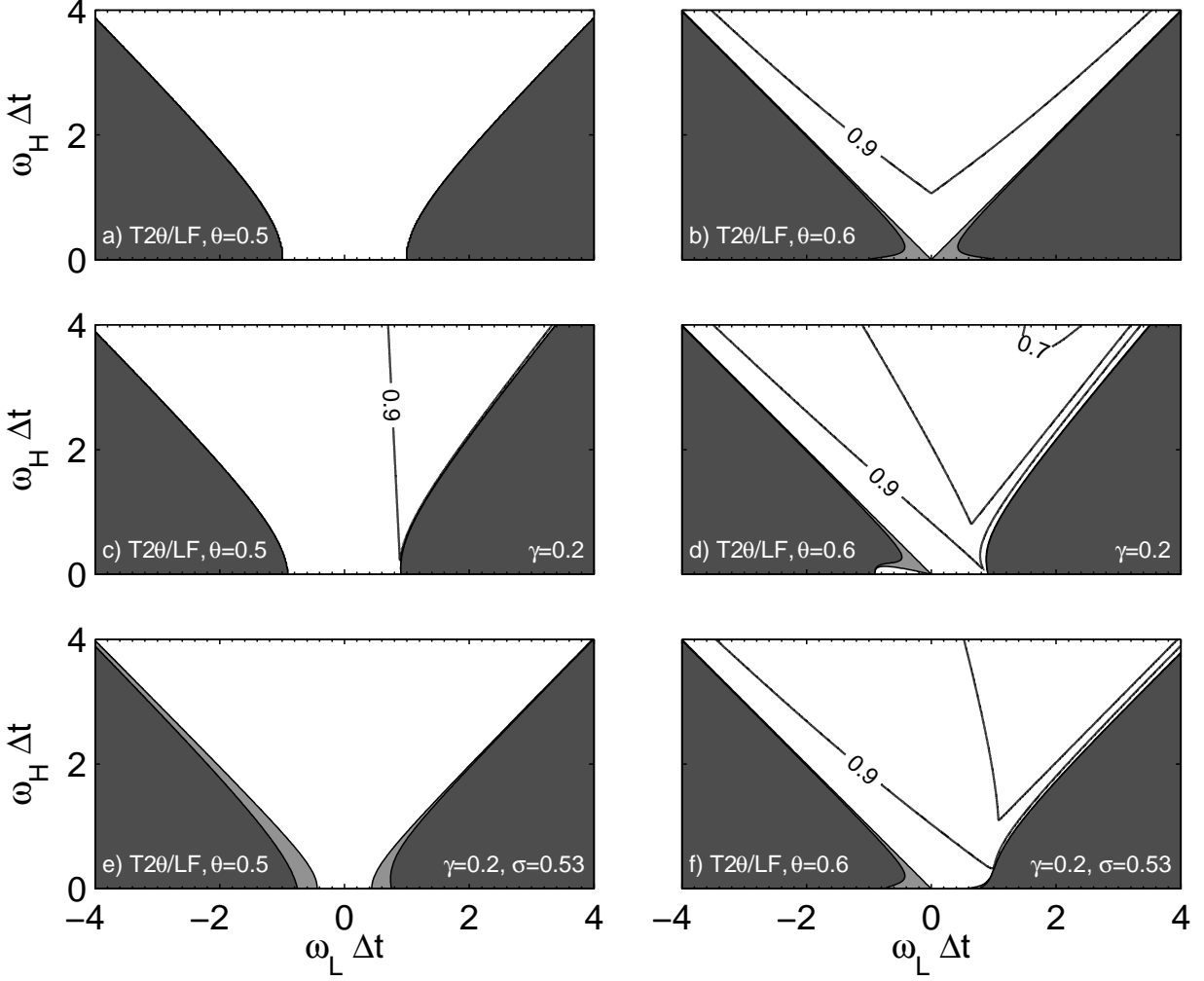


FIG. 5. Magnitude of the amplification factor for the leapfrog-based IMEX schemes listed in Table 1 for the model problem (12). The contour interval is 0.1, except that regions with $1 < |A| < 1.01$ are shaded gray and regions in which $|A|$ exceeds 1.01 are shaded dark gray. Only the upper half-plane is plotted, the values of $|A|$ in the lower half plane are anti-symmetric about the origin.

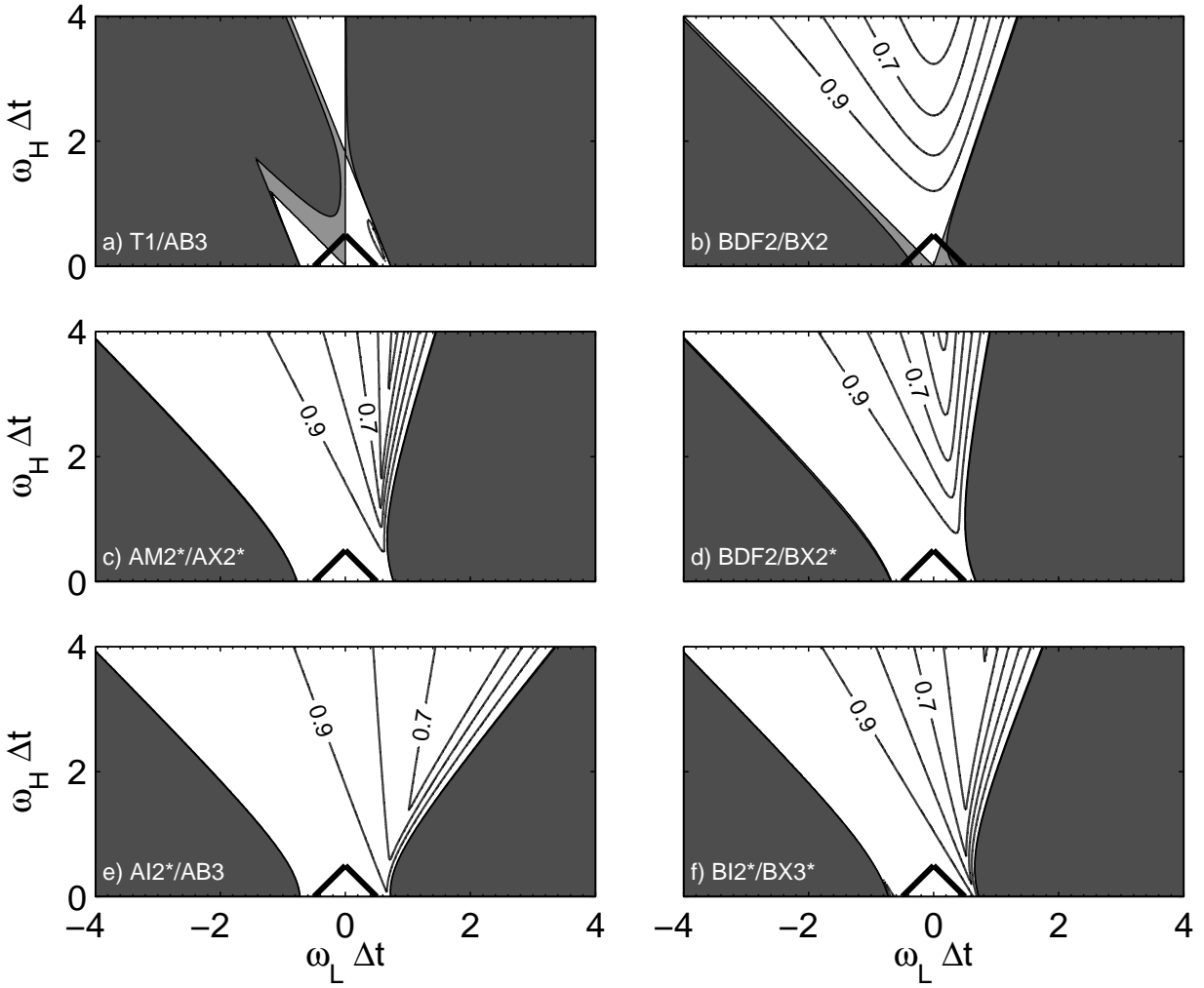


FIG. 6. As in Fig. 5 except for the Adams and the backward-differenced IMEX schemes listed in Table 1.

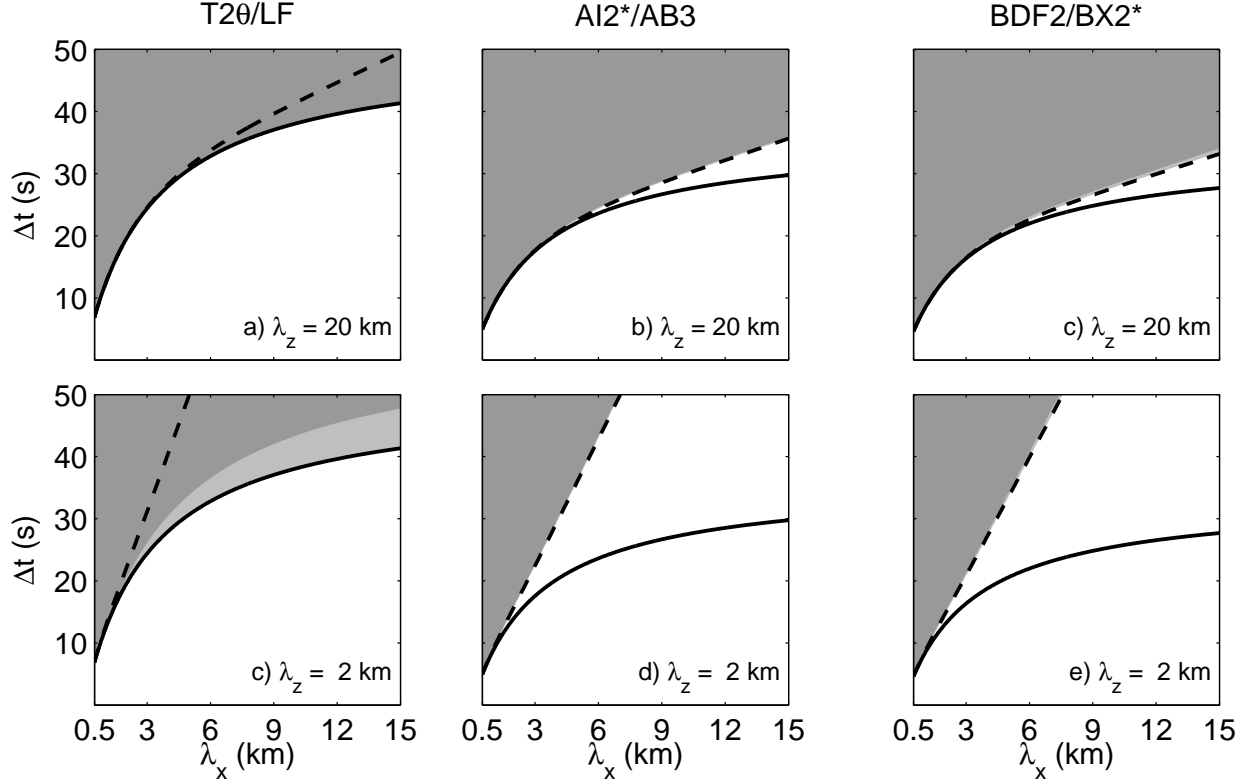


FIG. 7. Stable regions as determined from the maximum eigenvalue Ψ for wave solutions to the compressible Boussinesq equations using the IMEX decomposition (29). Ψ is contoured as function of horizontal wavelength and time step for modes with vertical wavelengths of 20 km (top row) and 2 km, bottom row. Values for the T2 θ /LF method are shown in the left column; those for the AI2*/AB3 method appear on the right. Regions with $0 \leq \Psi \leq 1$ are white, those with $1 < \Psi < 1.01$ are light gray and regions in which Ψ exceeds 1.01 are dark gray. Also plotted are the curves for $F_1(\lambda_x, \Delta t) = C$ (solid line) and $F_2(\lambda_x, \Delta t) = C$ (dashed); see text.

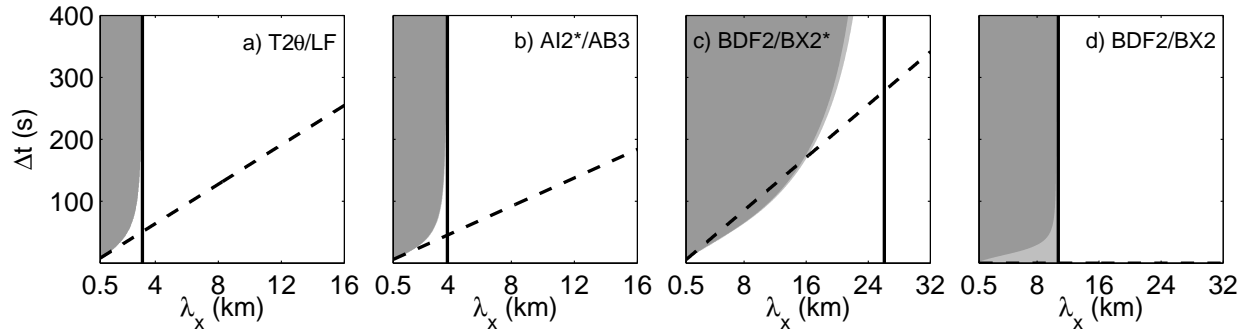


FIG. 8. Contours of Ψ indicating stable regions as in the first row of Fig. 7, except for the IMEX decomposition (34), and the addition of the BDF2/BX2 method in panel (d). Shading convections are as in Fig. 7. Note the horizontal scale in panels (c) and (d) is almost double that in (a) and (b). Also shown are the lines $\tilde{\omega}_L \Delta t = C$ (dashed) and $\tilde{\omega}_H / \tilde{\omega}_L = \xi$ (solid).

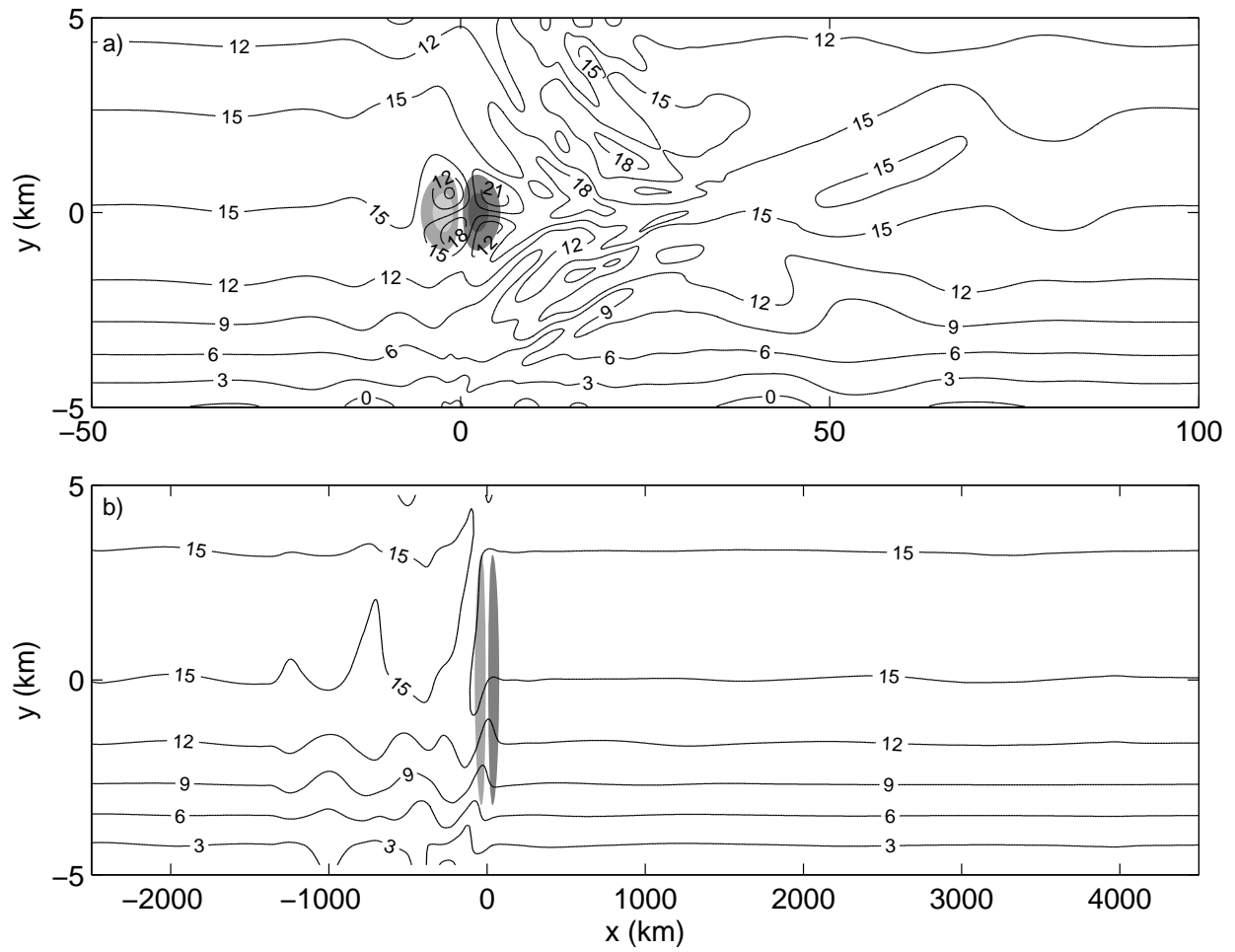


FIG. 9. Contours of the horizontal velocity at $t = t_d$ in the central portion of the domain for (a) case NH and (b) case H. Gray shades show contours of ψ with steps in the gray scale at ± 5 and $\pm 15 \text{ m}^2 \text{ s}^{-2}$ in case NH and $\pm 1 \text{ m}^2 \text{ s}^{-2}$ in case H.

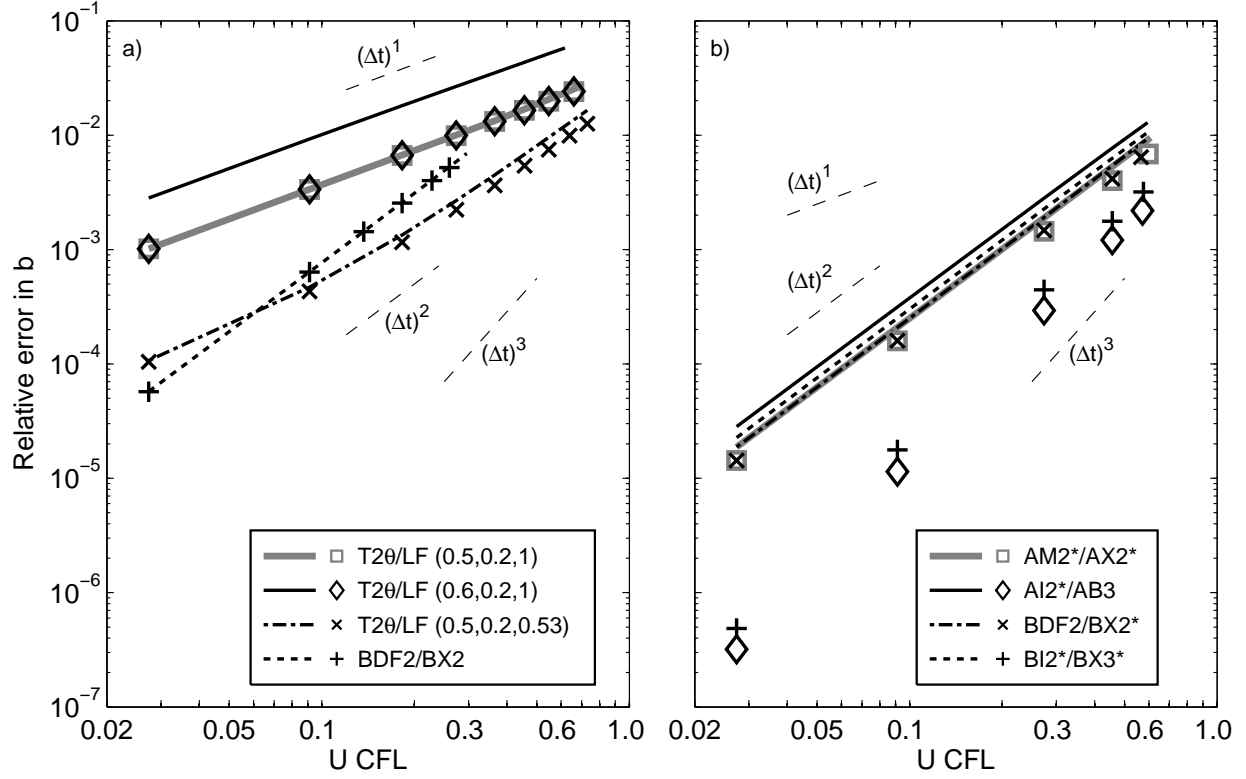


FIG. 10. Log-log plot of the error in the buoyancy field as a function of advective Courant number for the several of the methods listed in Table 1 for case NH. The curves show the result when buoyancy is treated implicitly; the symbols show the results when the buoyancy terms are approximated using the explicit part of the scheme. The lines/symbols terminate at the largest advective CFL number for which each method is stable. Thin dashed lines show the slopes corresponding to first, second and third-order convergence. The triplet of numbers after the T2 θ /LF methods denote the values of (θ, γ, σ) .

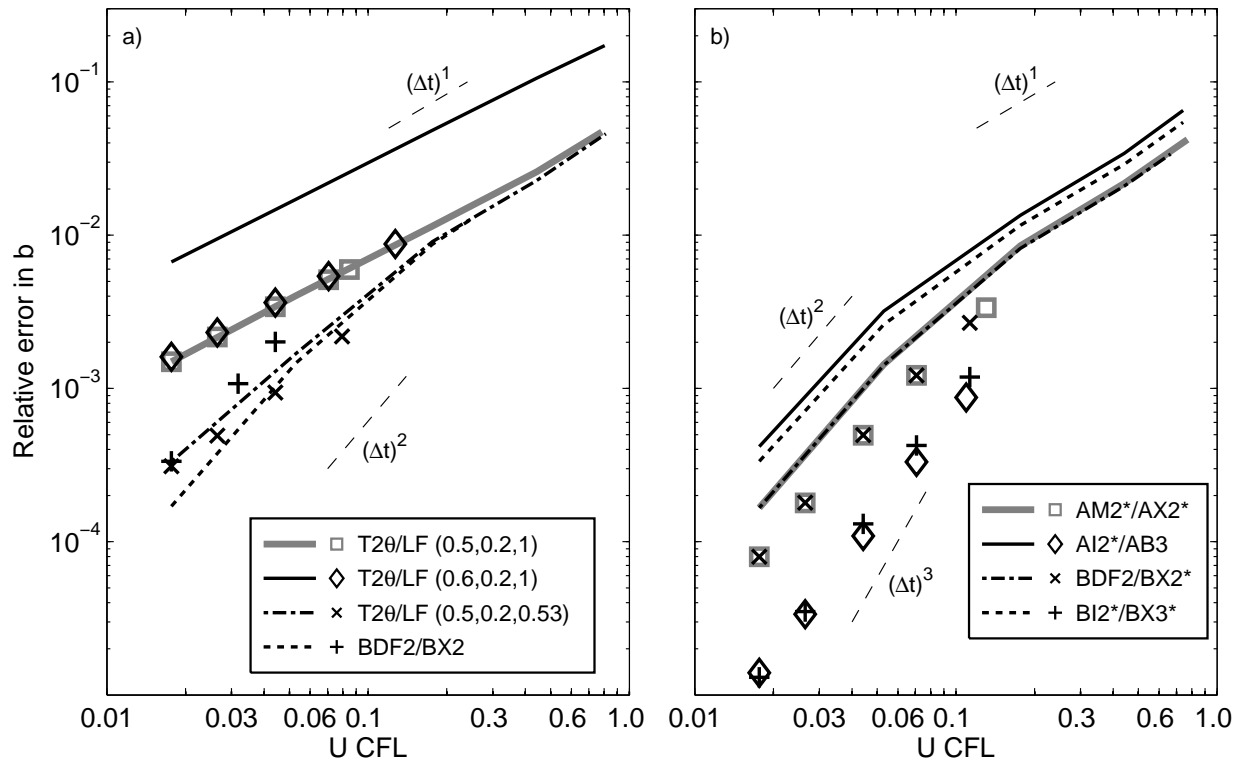


FIG. 11. As in Fig. 10 for case H.